

SCHOOL OF PHYSICS AND ASTRONOMY

YEAR 3 FINAL PROJECT REPORT

SESSION 2021-2022

Name:	Ashley Thean Voon Kit
Student Number:	C1900846
Degree Programme:	BSc Physics
Project Title:	Characterizing Arrays of Kinetic Inductance Detectors
Supervisor:	Dr. S. Doyle
Assessor	Dr. G Klemencic

Declaration:

I have read and understand Appendix 2 in the Student Handbook: "Some advice on the avoidance of plagiarism".

I hereby declare that the attached report is exclusively my own work, that no part of the work has previously been submitted for assessment (although do note that material in "Interim Report" may be re-used in the final "Project Report" as it is considered part of the same assessment), and that I have not knowingly allowed it to be copied by another person.

Acknowledgments

I would like to thank my supervisor, Dr. Simon Doyle for his continued support and guidance throughout this report, where this would not have been possible without it. Extra thanks for your patience in explaining many times over superconductivity theory.

Also, many thanks to Dr. Tom Brien for patiently explaining the detector in detail when I visited and for providing several diagrams and schematics of the KID used throughout this report.

Many thanks to Dr. Sam Rowe for guiding me through taking detector measurements, providing the filter transmission data and patiently explaining how the data measurement for the KID works.

I would also like to thank my partner Georgia for continuously supporting me throughout the long nights of working on this report.

Abstract

Millimetre-wave detection has many real-world applications such as in astronomy and in airport security cameras, but there is a gap in detector technology within this wavelength range. Kinetic inductance detectors (KID) have been developed to fill this gap, and one such KID system is the SFAB Airport Security Camera that is under development for commercial use. This report focuses on characterizing the SFAB system by exploring how a KID works through studying the principles of superconductivity and creating an ideal model of how a KID responds to a change in temperature. Using this knowledge, the first detector property which is the response of the detector, was found by taking measurements of a known temperature source and modelling it as a blackbody. Using this response and the detector noise the minimum signal detectable or the Noise-Equivalent-Power (NEP) can be determined as a measure of sensitivity. The mean NEP of the detector array, found to be $(5.0 \pm 0.5) \times 10^{-15} \text{ WHz}^{-0.5}$, was compared to the fundamental noise limit, where the array NEP was found to be 5.88 times larger. Finally, the KID array NEP was compared to other commercial detectors of various types, where the SFAB system was found to be the lowest NEP and thus gives confirmation that it is easier to create highly sensitive KID arrays.

Table of Contents

Acknowledgments	i
Abstract	ii
1. Introduction	1
1.1 Background	1
1.2 Kinetic Inductance Detectors	2
1.3 Characterizing Detector Systems	3
1.4 Aims and Objectives	4
2. Kinetic Inductance Detector Theory	5
2.1 Principles of Superconductivity	5
2.2 How a KID Works	10
2.3 Ideal KID Simulation	14
3. Methodology	17
3.1 Data Acquisition and $dF0$	17
3.2 Modelling the Hot Bar Power, dP	21
3.3 Detector Response	24
3.4 Noise-Equivalent-Power	30
4. Results and Discussions	34
4.1 Analysis of Results	34
4.2 Implications on the System	36
4.3 NEP Contributions and Noise Sources	37
6. References	42

1. Introduction

1.1 Background

Millimetre-wave detection has many real-world applications such as in astronomy and airport security cameras. For airport security cameras, their aim is to identify concealed objects beneath clothing, illustrated below:



Figure 1 [17] Imaging concealed objects labelled A, B, C, by SFAB system

The frequency at which this can be observed, is ~ 280 GHz or a wavelength of ~ 1 mm.

Various detector types such as bolometers, heterodyne receivers and semiconductor technology have been designed for mm-wave range and perform well. However, the mentioned detectors still have several limitations as shown in the table below:

Detector Type	Limitations
Semi-conductor technology	Limited to wavelengths down to $\sim 70\mu\text{m}$
Heterodyne receivers	Typically noisy and not practical for large format imaging arrays
Bolometers	Have sensitivity but poor multiplexing

Table 1: Limitations of detector types for mm-wave detection [17]

Table 1 shows that 2 challenges arise from mm-wave detection, limited array size and wavelength range. The array size is typically limited due to impracticality and difficulties in multiplexing, which is a method used to combine multiple signals into a singular signal.

The other limitation is the wavelength range for semiconductor technology detectors. Semiconductor type detectors detect by having photons provide energy to excite electrons from the valence band to the conduction band. The minimum energy required is known as the bandgap energy, thus also the minimum detectable photon energy. The semiconductor material with the lowest bandgap energy is InSb, at 0.017eV [18], which is a photon wavelength of $72\mu m$. As such, semiconductor technology detectors are limited to wavelengths shorter than $72\mu m$, leaving a gap in the technology below $72\mu m$.

1.2 Kinetic Inductance Detectors

Kinetic Inductance Detectors (KID) are an emerging technology that has gathered interest as KIDs provide practical solutions to the challenges faced by mm-wave detection mentioned previously. KIDs are a type of photodetector that operate based on the microwave properties of superconductors. As the name suggests, the response of the detectors is measured from its kinetic inductance, which is a property that emerges from superconductivity. Detection happens when a photon is incident, which will change its kinetic inductance. This allows the detection of the photon in a resonant LC circuit in the detector as it responds to the change in kinetic inductance, where the change in resonant frequency can be measured and related to the response of the KID.

KIDs address the limited wavelength range as its gap energy is $\sim 10^{-3} eV$ [19], equating to photon wavelengths of $\sim 3mm$, which is significantly longer. KIDs also address the limited array size, as they are compact and can create large detectors arrays easily. It also has excellent multiplexing ability and remarkable sensitivity. As a result, KID systems are easier to create large arrays, as shown:

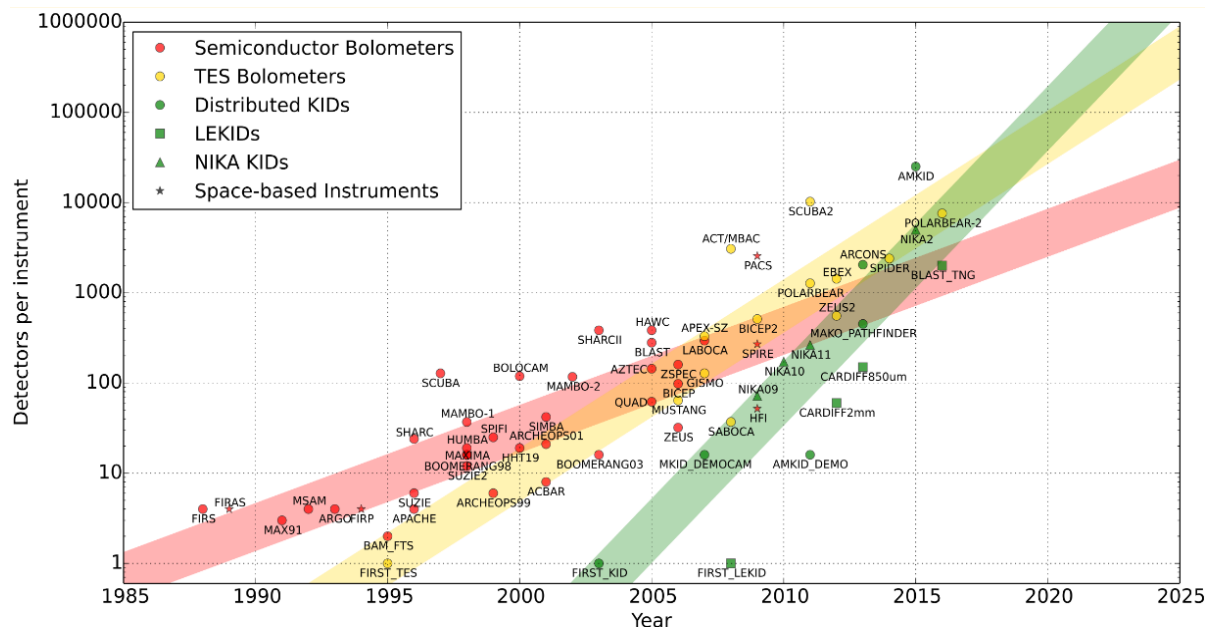


Figure 2 Graph from 2016 of instrument detector counts vs year, with trendlines for Semiconductor-based Bolometers (red), superconductor-based bolometers (yellow) and KIDs (green). [17]

Figure 2 shows that KIDs outpace the other detector types in terms of instrument detector counts due to the reasons above. To provide further comparisons between the detector types, the KID system can be characterized using different performance metrics detailed in the following section.

1.3 Characterizing Detector Systems

To compare the performances, various performance metrics or detector properties can be used to judge its effectiveness. These properties give valuable insight into the performance, limitations, strengths and optimization potential of the system. This report aims to quantify four detector properties:

- Responsivity, R

A measure of the response magnitude and gives the input-output gain of a detector system [2]. This is given by the ratio of a physical property change of a detector dx , such as electrical output for semiconductors type detectors, to the input optical power dP :

$$R = \frac{dx}{dP} \quad (1)$$

As mentioned, KIDs measure response from the change in resonant frequency dF_0 . The R of a KID, R_{KID} , is therefore:

$$R_{KID} = \frac{dF_0}{dP} \quad (2)$$

- Noise Spectral Density, e_n

A frequency distribution for the mean-squared value of the noise power. It is calculated as a power spectral density (PSD) or the mean-square fluctuation per unity frequency range [2]. This allows the characterization of the noise of the detector by the features of the spectrum and identification of the noise sources.

e_n is calculated by taking a Fourier Transform of the time ordered detector output to create a noise spectrum in the frequency domain.

- Noise-Equivalent-Power (NEP)

The NEP is defined as the incident signal power on the detector that yields a signal-to-noise ratio of 1 in 0.5 seconds of photon collection time. For an ideal detector, the fundamental limit of noise, sets

the limit on the minimum detectable power, which is attributed to the sensitivity. This minimum detectable power is known as the photon noise limited NEP, NEP_{ph} [2].

When detecting small amounts of optical power, the background noise usually dominates the output of a detector and will mask the output that is produced by a weak signal due to its random fluctuations, which the signal can be said to be background dominated. This diminishes the ability for small amounts of optical power to be detected. As such, the background noise sets the limit on the minimum spectral flux that can be detected. This minimum power detectable is known as the NEP and is a quantification of a detector's sensitivity for real measurements [2]. The NEP can be expressed based on the e_n and the response R [2]:

$$NEP = \frac{\sqrt{e_n}}{R} \quad (3)$$

- Detector Yield

A quantity representing the percentage of the number of detectors that gave a resolvable response $n_{responsive}$ to the total number of detectors n_{KID} :

$$Yield = \frac{n_{responsive}}{n_{KID}} \quad (4)$$

1.4 Aims and Objectives

The aim of this report is to characterize the SFAB Airport Security Camera, a KID system in development by the Detector team in Cardiff University, in terms of its detector properties.

The objectives of this report are listed as follows:

1. Understand the principles of superconductivity and its application to KIDs
2. Use this knowledge to create a simulation of an ideal KID for a change in temperature
3. Measure a source of known temperature and quantify the detector response from the data
4. Compared this response to detector noise to determine minimum signal detectable (NEP)
5. Perform a statistical analysis of NEP for all the KIDs in the array and compared it to the fundamental noise limit

2. Kinetic Inductance Detector Theory

KIDs operate based on the microwave properties of superconductors as mentioned. This chapter explores principles of superconductivity and its application to KIDs, along with a simulation of how an ideal KID responds to a change in temperature.

2.1 Principles of Superconductivity

For superconducting materials below a critical temperature T_c , the DC resistance falls to zero. This zero resistance can be attributed to a new path for the current that flows through the new density of superconducting electrons n_s . Bardeen, Cooper and Schrieffer explain this in the BCS Theory [3]. When temperatures decrease below T_c , electrons start to form pairs known as Cooper-pairs with a binding energy of 2Δ . An important property of these pairs is that they do not scatter in the material, giving the property of zero resistance which superconductors are known for.

Following this, the conductivity of the superconductor can be expressed using the Drude Model based on Ashcroft and Mermin, which explains that the conductivity of a metal σ_n can be expressed as [4]:

$$\sigma_n = \frac{n_n e^2 \tau}{m(1 - j\omega\tau)} \quad (5)$$

Where n_n is the normal electron (quasi-particle) density, j equals to $\sqrt{-1}$, and τ is the scattering time, m is the mass of the electron, e the elementary charge and ω is the angular frequency.

From this, F. London and H. London put forward explanations for the behaviour of electrons in superconductors, giving an expression for the conductivity of the Cooper-pair electron density n_s when τ approaches ∞ as they do not scatter [5]:

$$\sigma_s = -j \frac{n_s e^2}{\omega m} \quad (6)$$

It can be observed that the expression σ_s only comprises of imaginary terms, which will be further explored later in this section, under the Two Fluid Model.

Meissner Effect

Another important property of superconductors is the Meissner Effect, where the bulk of a superconductor expels any magnetic field or displays complete diamagnetism. London explains that superconductors cannot be modelled as perfect conductors due to the complete diamagnetism

property. The solution was to derive an expression for the magnetic field B as a function of the depth beneath the surface of the material x [5]:

$$B(x) = B(a) \exp \left(\frac{-x}{\sqrt{m/\mu_0 n_s e^2}} \right) \quad (7)$$

where $B(a)$ is the magnetic field at the surface. Equation 6 and 7 are collectively known as the London Equations, derived from the observed effects of superconductors and not the fundamentals.

Below the material surface, the magnetic field will fall to $1/e$ of the value of $B(a)$ when at a distance $\sqrt{m/\mu_0 n_s e^2}$. This distance is known as the London Penetration Depth (LPD) λ_L [5]:

$$\lambda_L = \sqrt{\frac{m}{\mu_0 n_s e^2}} \quad (8)$$

λ_L is used for characterizing the effects of photons on superconductors such as a KID.

Two Fluid Model

Following from the formation of Cooper-pairs, Gorter and Casimir [6] explains that the 2 electron populations n_s and n_n gives rise to the Two Fluid Model of superconductors. The model considers that a current in a superconductor will have 2 paths it can propagate: the 2 populations. From [2], temperature dependence of ratio n_s/n is given by:

$$\frac{n_s}{n} = 1 - \left(\frac{T}{T_c} \right)^4 \quad (9)$$

and

$$n_n = n - n_s \quad (10)$$

n_s is inversely proportional to temperature T , whereas n_n also falls due Cooper-pair formation. This relationship can be observed below:

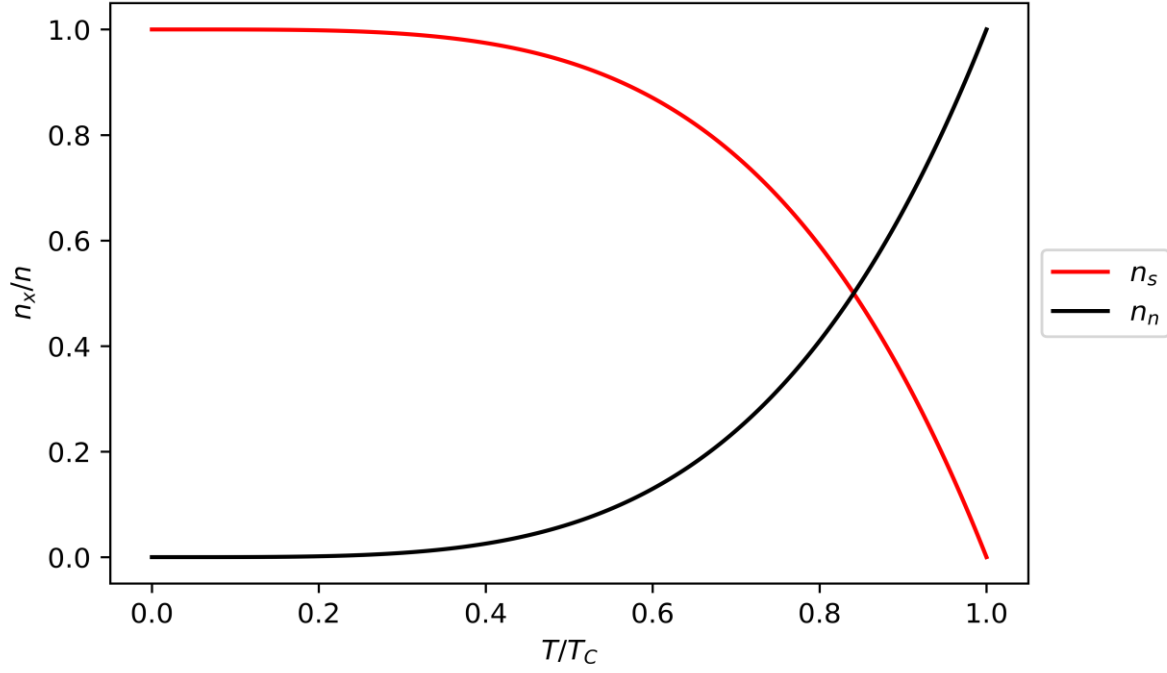


Figure 3 Graph of ratio of n_s and n_n to total electron population n vs the ratio of T to T_C

This relationship will be useful in modelling a KID as its response is dependent on the populations, shown in [7].

The variation in n_s with T means that λ_L also varies with temperature. The expression for λ_L as a function of T can be obtained with Equation 9 and 10:

$$\lambda_L(T) = \lambda_L(0) \left[1 - \left(\frac{T}{T_C} \right) \right]^{-0.5} \quad (11)$$

where $\lambda_L(0)$ is the LPD at 0K.

For this report, the effect of varying temperature is used to model detection. Fundamentally, increasing temperature has the same effect as incident photons, KID as it provides energy to break Cooper-pairs. The detection of the KID is modelled by temperature changes instead of photon counting as it simplifies the model.

[7] provides an explanation for the effects of varying frequencies incident on a superconducting material; From Equation 6, at low frequencies, σ_s is far greater than σ_n . However, at higher frequencies, especially in the microwave region, σ_n is no longer negligible. This is attributed to an inertia of n_s as the energy drawn from electric field E is stored as kinetic energy, and this inertia produces a reactance which gives a large impedance at high frequencies. As such, this stored kinetic energy relates to the kinetic inductance of n_s . The effect also causes the current J_s to lag E by 90° , which explains why σ_s only comprises of an imaginary part. This increase in σ_n with σ_s decrease leads to a larger proportion of J flowing through the resistive quasi-particle path at higher frequencies. This can be illustrated in a circuit-equivalent diagram in Figure 2:

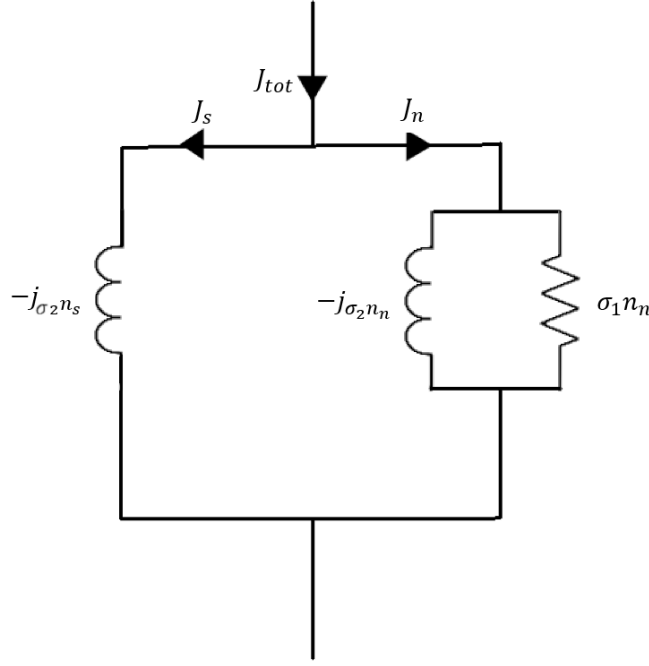


Figure 4 Circuit-equivalent diagram of J through n_s and n_n at high frequencies

Internal Inductances

A KID measures a detection through a change in the internal inductance. Building on previous sections, [7] explains that the inductances of a superconducting material can be characterized as it changes with temperature as does λ_L . Kinetic inductance is associated with the kinetic energy of n_s and magnetic inductance L_m is due to the magnetic field energy density by J_s stored in the volume. The derivation is lengthy and beyond the scope of the project, as such we quote [7] for the inductance expressions:

$$L_k = \frac{\mu_0 \lambda}{4W} \left[\coth\left(\frac{t}{2\lambda}\right) + \left(\frac{t}{2\lambda}\right) \operatorname{cosec}^2\left(\frac{t}{2\lambda}\right) \right] \quad (12)$$

and

$$L_m = \frac{\mu_0 \lambda}{4W} \left[\coth\left(\frac{t}{2\lambda}\right) - \left(\frac{t}{2\lambda}\right) \operatorname{cosec}^2\left(\frac{t}{2\lambda}\right) \right] \quad (13)$$

where t is the thickness. The internal inductance L_{int} is simply the sum of the inductances. Quoting from [2]:

$$L_{int} = L_k + L_m = \frac{\mu_0 \lambda}{2} \coth\left(\frac{t}{2\lambda}\right) \quad (14)$$

where L_{int} is in per unit square. Note, L_k and L_m are in per unit length; by setting length = W, the W term can be eliminated from *Equations 12 and 13*, giving in per unit square.

Since $L_{int} \propto \lambda$ and $\lambda \propto n_s$ from *Equation 8 and 14*, absorbed photons will break Cooper pairs and decrease n_s leading to a change in L_{int} that can be detected through a change in resonant frequency of an LC circuit that forms the detector.

Mattis-Bardeen Theory

As mentioned earlier, the results derived for the conductivity is not based on any fundamentals of superconductivity. In BCS Theory, the band gap is not introduced, and the electrons are accelerated independently if E applied whereas due to finite size of Cooper-pairs, it is not the case. This description is instead given by the Mattis-Bardeen Theory [8]. Pippard gives a non-local treatment of the London Equations from the Mattis-Bardeen Theory, leading to the Mattis-Bardeen Approximations, for $k_B T \ll \Delta(0)$ [9]:

$$\frac{\sigma_1}{\sigma_n} = \frac{2\Delta(T)}{\hbar\omega} \exp(-\Delta(0)/k_B T) K_0(\hbar\omega/2k_B T) [2 \sinh(\hbar\omega/2k_B T)] \quad (15)$$

and

$$\frac{\sigma_2}{\sigma_n} = \frac{\pi\Delta(T)}{\hbar\omega} [1 - 2\exp(-\Delta(0)/k_B T) \exp(-\hbar\omega/2k_B T) I_0(\hbar\omega/2k_B T)] \quad (16)$$

I_0 and K_0 are the modified Bessel functions of the first and second kind respectively. σ_n is the normal state conductivity, $\Delta(T)$ is the temperature dependent binding energy, and $\Delta(0)$ is the binding energy at 0 K.

$\frac{\sigma_1}{\sigma_n}$ and $\frac{\sigma_2}{\sigma_n}$ can be plotted against T to show the temperature variation using *Equation 15 and 16*:

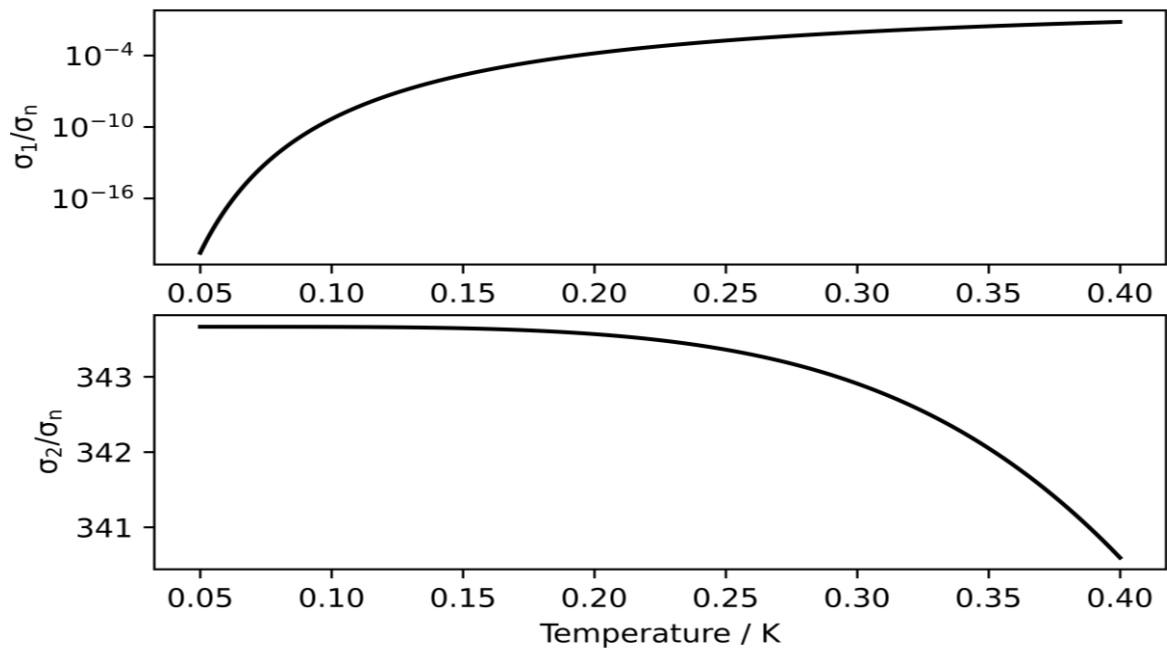


Figure 5 $\frac{\sigma_1}{\sigma_n}$ and $\frac{\sigma_2}{\sigma_n}$ against T for an Aluminium sheet at 7GHz

By using σ_2 from the Mattis-Bardeen Approximations, combined with the real part of *Equation 5* for σ_2 and *Equation 8* for λ , the Mattis-Bardeen LPD $\lambda_{MB}(T)$ is found:

$$\lambda_{MB}(T) = \sqrt{1/(\mu_0 \sigma_2 \omega)} \quad (17)$$

Using *Equation 14,16 and 16*, a graph of L_{int} against T can be obtained:

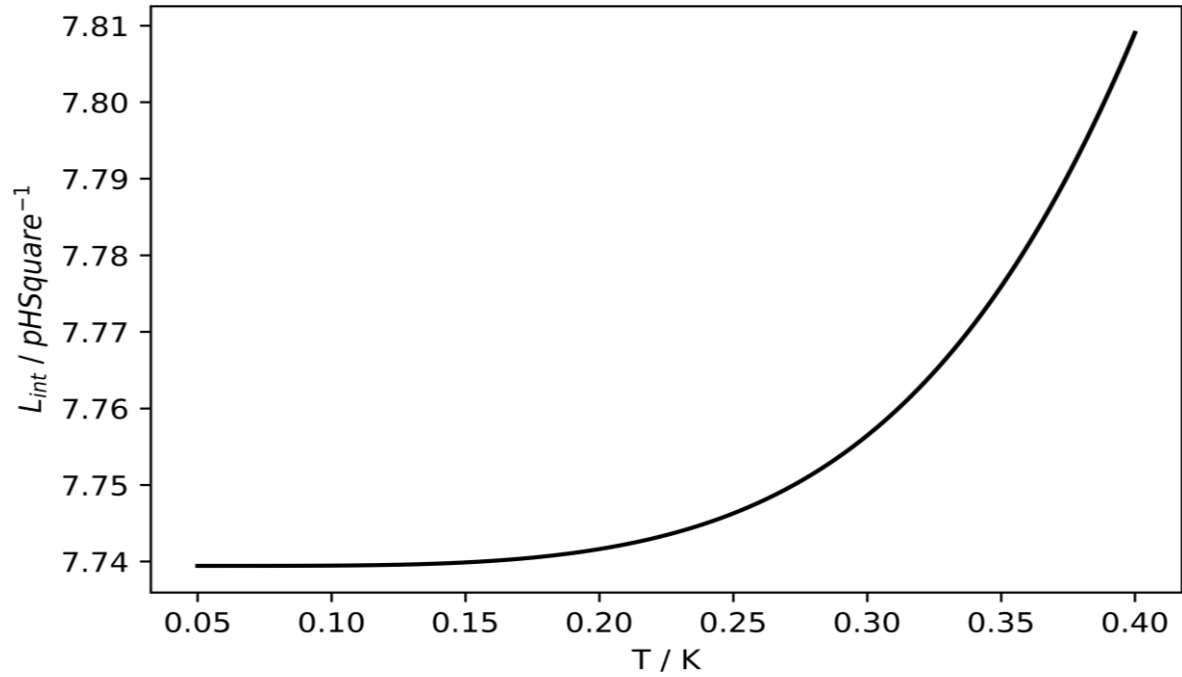


Figure 6 L_{int} variation with T for an Aluminium sheet at 7GHz using Mattis Bardeen Approximations

[7] shows that the resistance of a superconducting strip can then be calculated from the real part of the impedance:

$$\text{Resistance} = L_k \omega \frac{\sigma_1}{\sigma_2} \quad (18)$$

2.2 How a KID Works

Schematic

With the fundamentals, it is now possible to explore how a KID works. The detection of photons is accomplished on a KID Resonant Circuit. It is a circuit etched on an aluminium sheet on a silicon wafer [21]. A schematic is shown below:

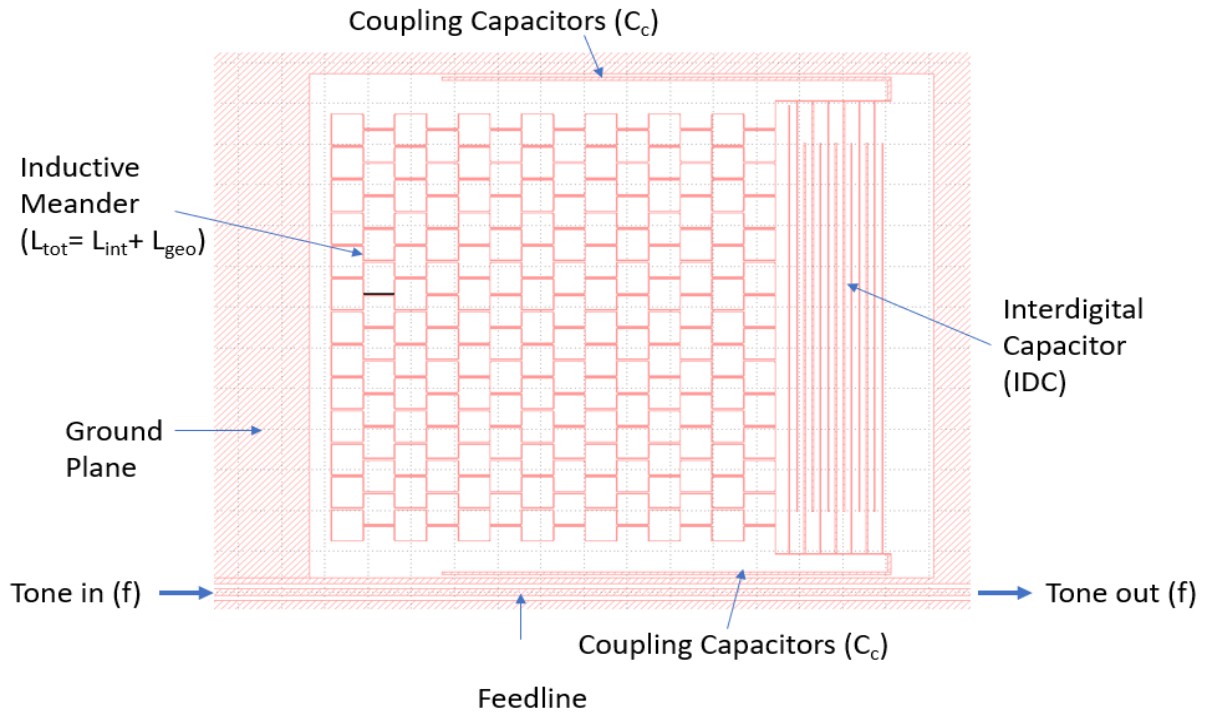


Figure 7 [21] Schematic of a single KID, with an aluminium sheet (Dashed) which contains the circuit on a silicon wafer (white)

The detector operates at $\sim 270 \text{ mK}$ [7], well below T_C . The inductive meander has a total inductance $L_{tot} = L_{int} + L_{geo}$, coupled to the interdigital capacitor IDC. The geometric inductance, L_{geo} is material and geometry dependant, since these quantities is constant throughout, L_{geo} will be taken as a constant. The circuit behaves as an LC circuit that has resonant frequency ω_0 . The diagram can be illustrated as a circuit diagram as shown:

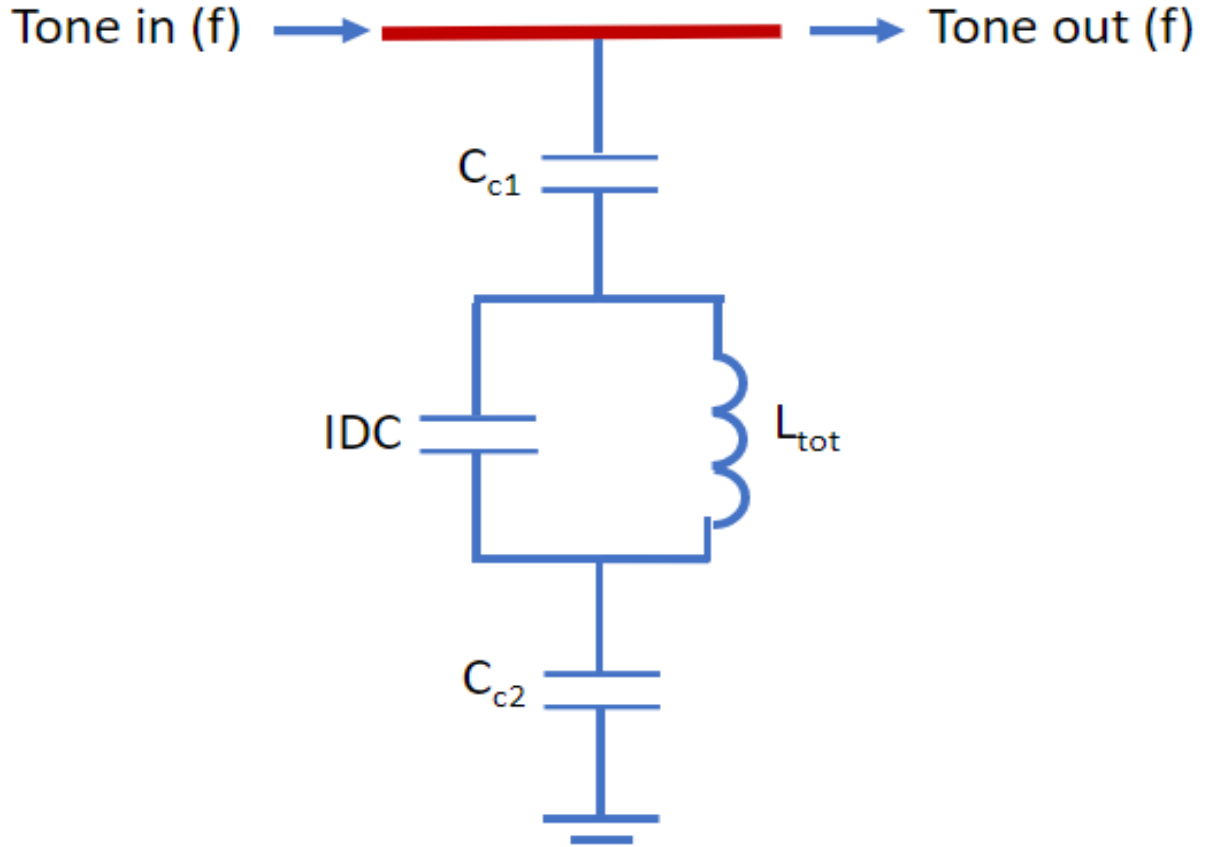


Figure 8 [21] Circuit diagram of the KID resonant circuit where L_{tot} is the inductive meander

There are 2 coupling capacitors, the first coupling capacitor C_{c1} is coupled to the transmission feedline and the second C_{c2} is coupled to ground. [21]

When a photon is incident on the detector, it provides energy for Cooper-pairs to overcome Δ . n_s decreases as Cooper-pairs break, and therefore L_{int} will vary according to *equation 14* and L_{tot} varies as well.

The capacitance C_c of the coupling capacitors and the total capacitance C_{tot} is given [21]:

$$C_c = \frac{C_{c1}C_{c2}}{C_{c1} + C_{c2}} \quad (19)$$

and

$$C_{tot} = IDC + C_c \quad (20)$$

As mentioned, the circuit is modelled as an LC circuit with a resonant frequency that can be found with C_{tot} from *Equation 20* and L_{tot} :

$$\omega_0 = \frac{1}{\sqrt{L_{tot}C_{tot}}} \quad (21)$$

Since L_{tot} varies with respect to photon intensity on the inductive meander, ω_0 varies accordingly. ω_0 is coupled to the transmission feedline, thus a change in the frequency can be measured.

Microwave Electronics Readout

[20] explains a common phenomenon faced by microwave electronics, such as KIDs, where electronic components' dimensions become comparable to signal wavelengths. Therefore, treatment of the signal must be of a wave instead of voltage and currents. An illustration is shown below:

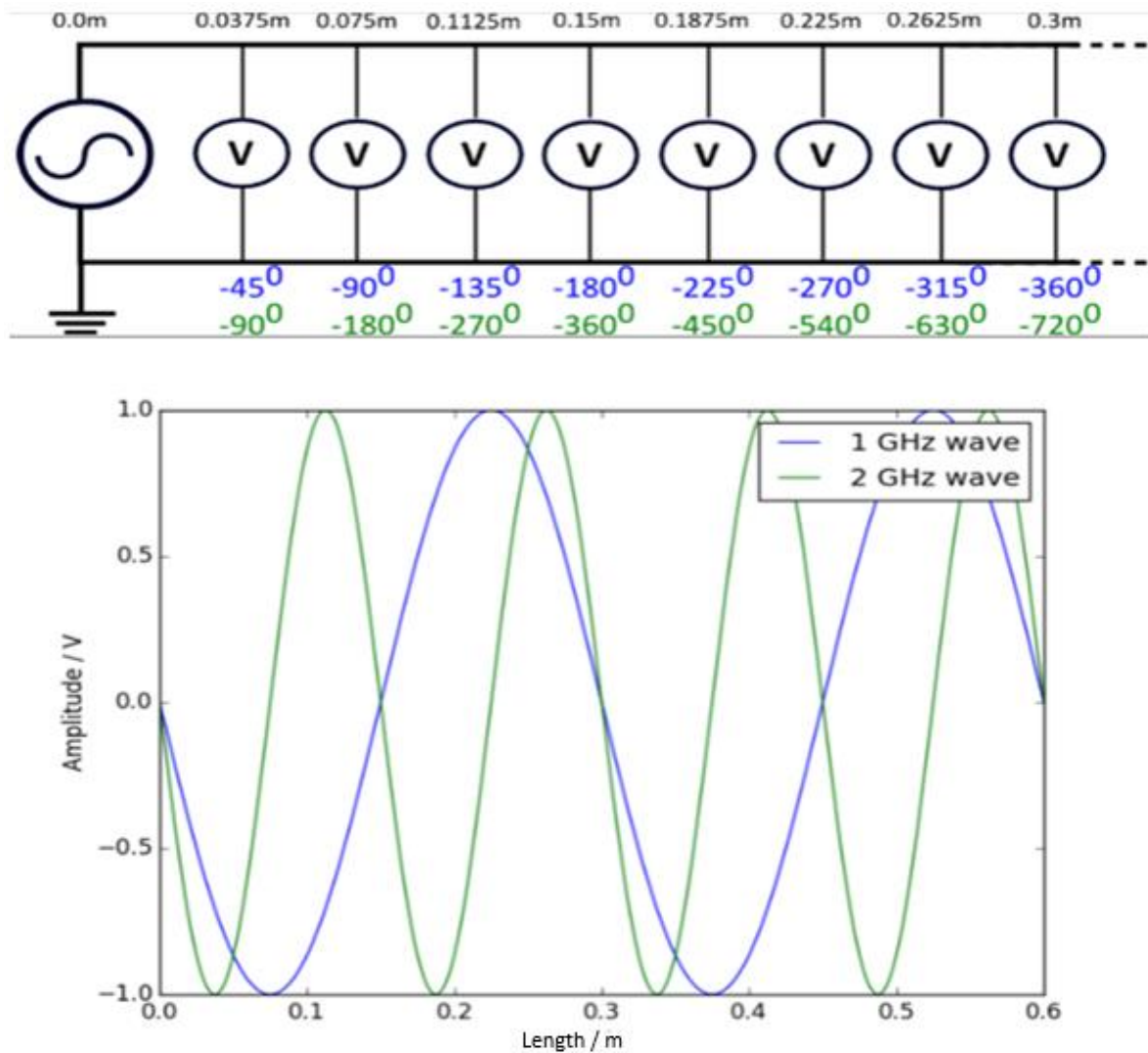


Figure 9 [20] Diagram illustrating phase difference of microwave frequency readouts at different length of a wire

As such, it is useful to define a microwave circuit based on scattering parameters, defined as the ratio of voltages on 2 ports [20]. For a KID it is the ratio of input signal through the feedline into the

KID to output signal, noted as S21. Its derivation is beyond the scope of this project, therefore the expression for S21 is quoted from [10], expressed as an amplitude $|S_{21}|$ and phase ϕ_{s21} :

$$|S_{21}| = \sqrt{Q^2 + I^2} \quad (22)$$

and

$$\phi_{s21} = \text{Arctan}\left(\frac{Q}{I}\right) \quad (23)$$

where I and Q is the real and imaginary component of S21 respectively. A KID will measure and output I and Q values in units of Volts, which we can relate to a change in ω_0 .

2.3 Ideal KID Simulation

Combining the microwave properties of superconductors and the KID resonator circuit readout, it is now possible to model a KID with temperature variation, corresponding to a detection. The model was created using Python with several values quoted as constant parameters for a detector being tested in SFAB:

- $L_{geo} = 55.6 \times 10^{-9} H$
- *Tone Frequency* $F_0 = 0.95 GHz$
- *Number of squares* $= 27223$
- $C_c = 1.5 \times 10^{-14} F$
- *Critical Temperature of Aluminium Sheet* $T_c = 1.5 K$
- *Normal State Conductivity of Material*, $\sigma_n = 6.0 \times 10^7 \Omega^{-1}m^{-1}$
- *Thickness of Superconducting Sheet*, $t = 20 nm$

The $\Delta(0)$ is defined as follows [7]:

$$\Delta(0) = \frac{3.5k_B T_c}{2} \quad (24)$$

$\Delta(T)$ approximated to a fixed value $\Delta(0)$ since dT is small and has insignificant changes to $\Delta(T)$.

The model was created using the principles of superconductivity and microwave electronics readout considerations. The resulting plot is as follows:

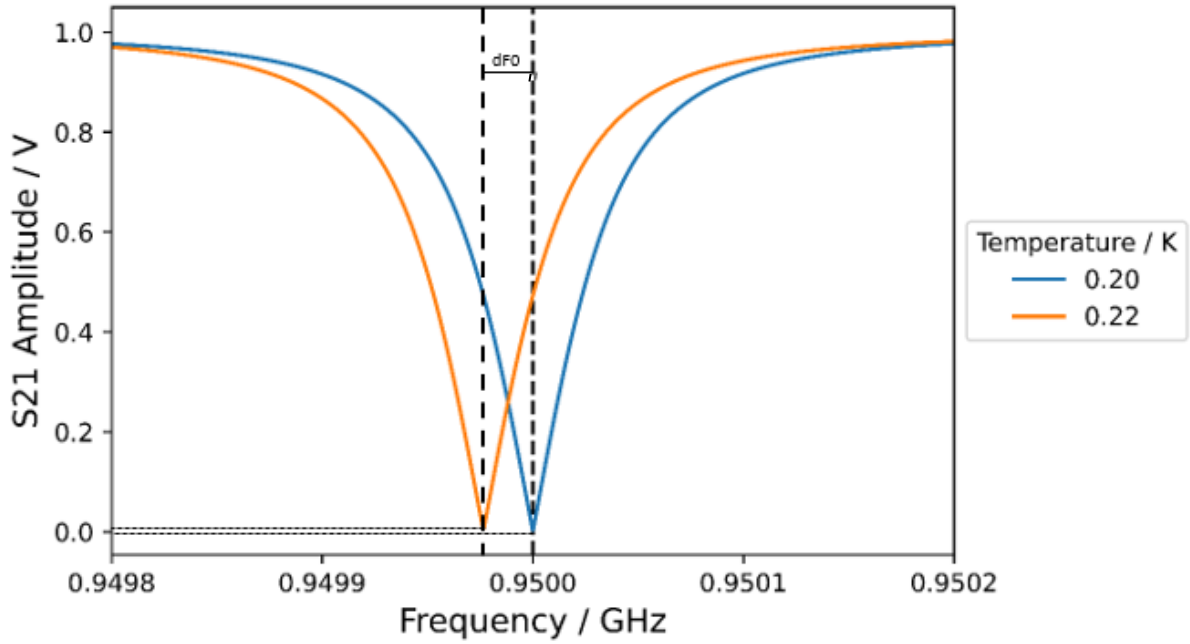


Figure 10 Tone Frequency variation of a single KID for 2 temperatures with the fixed parameters given above, with dF_0 labelled. For real measurements, plots like these where $|S_{21}|$ plotted against frequency is known as Sweep data/plots.

The shift in tone frequency, dF_0 for the minimum of $|S_{21}|$ corresponds to photon detection as increasing temperature changes F_0 . For constant resistance system, the $|S_{21}|$ does not vary with temperature and will be the same as the base temperature (lowest), the increase is due to varying resistance contributing to loss.

An intuitive way of understanding the I and Q variations is by plotting I vs Q for varying temperatures:

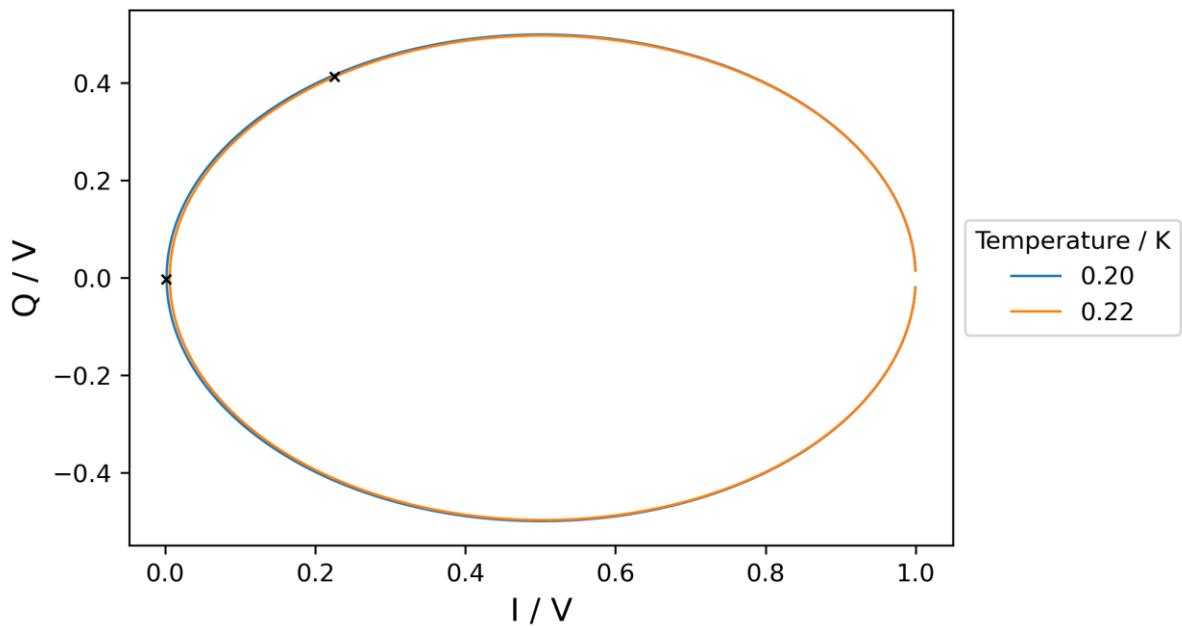


Figure 11 I vs Q plot for 2 temperatures. Crosses represent the I and Q values to corresponding temperature plot at F_0 .

Figure 11 shows the shift I and Q for different temperatures, where the cross represents a shift in I and Q at frequency F_0 . In real KID measurements, the data typically consists of I and Q values for both the sweep and time-streams (across time) for a set F_0 . Figure 11 illustrates how the I and Q values vary at the tone frequency, and ∂F_0 can be related to the response of the detector.

Since the KID is measured with a fixed tone, ∂F_0 needs to be inferred from I and Q data. A formula that considers changes in I $\partial I(t)$ and Q $\partial Q(t)$ time-stream data, from the base temperature or tone frequency, can be used to find ∂F_0 [20]

$$\partial F_0 = \frac{\partial I(t) \frac{\partial I}{\partial F} + \partial Q(t) \frac{\partial Q}{\partial F}}{\left(\frac{\partial I}{\partial F}\right)^2 + \left(\frac{\partial Q}{\partial F}\right)^2} \quad (25)$$

$\frac{\partial I}{\partial F}$ and $\frac{\partial Q}{\partial F}$ can be calculated by taking numerical derivatives at the minimum point of tone frequency or the base temperature in the sweep data.

Equation 25 is crucial, as it allows for the conversion of I and Q measurements of time-stream and sweep data, to ∂F_0 . The ∂F_0 quantifies the detection and is important in characterizing the responsivity in Equation 1.

Equation 25 holds well for small deviations in F_0 , after which the formula starts to deviate from real data. This limit can be observed by plotting the formula along with the minimum of $|S_{21}|$ from the model. This is shown below:

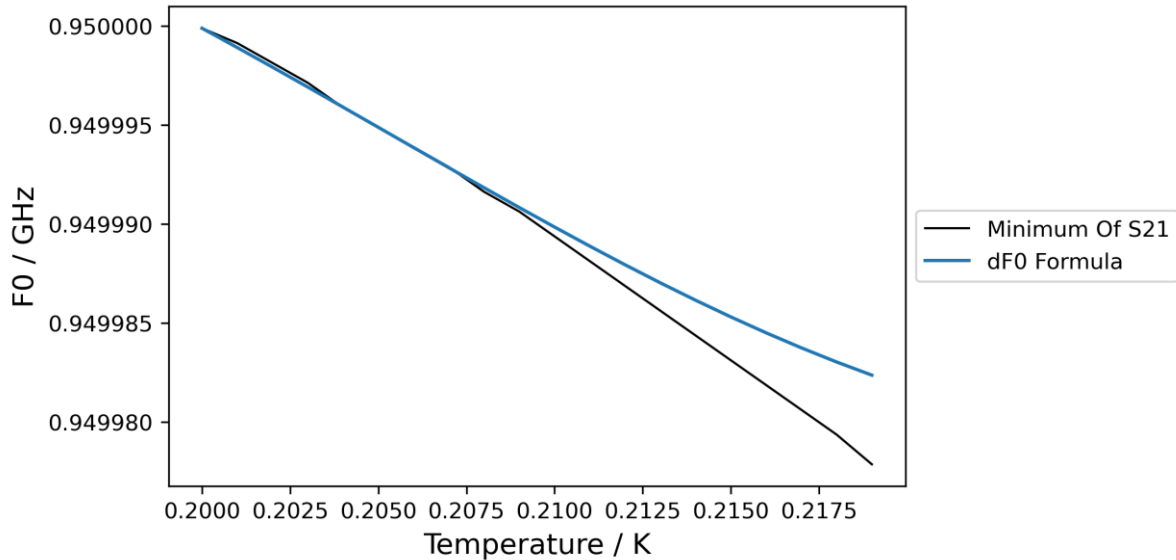


Figure 12 ∂F_0 formula plotted alongside the minimum of $|S_{21}|$ from the model for varying T

Figure 12 shows that the ∂F_0 formula holds remarkably well up till 0.21K. As such, the ∂F_0 formula is appropriate for low temperature variations, therefore the maximum change in F_0 for the approach to still be valid is $\pm 10000\text{Hz}$. This gives the maximum variation in F_0 when taking measurements.

3. Methodology

3.1 Data Acquisition and dF_0

To determine the detector properties, R must first be determined using *Equation 1*. This is achieved by taking measurements of a known temperature source and measuring the dF_0 . From there, dP can be found from modelling the spectral emission for it, explained further in section 3.2.

To measure the known temperature source, the detector system was set up as shown:

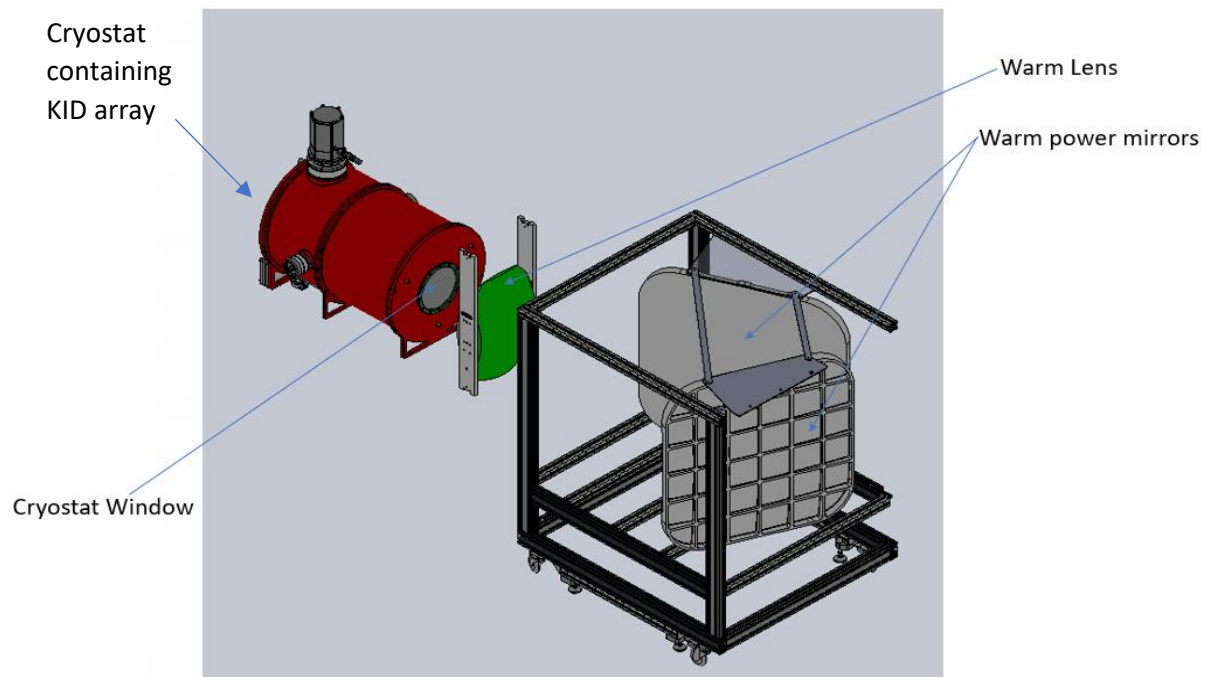


Figure 13 [22] Set up of the KID system with instruments labelled

The lens is used to focus the incident rays and the mirrors are to reflect the rays into the lens. The known temperature source was set up as a hot bar electrically warmed. The hot bar was placed in front of the detector system with foam padding behind it to limit the variation in background optical power. The setup is shown:

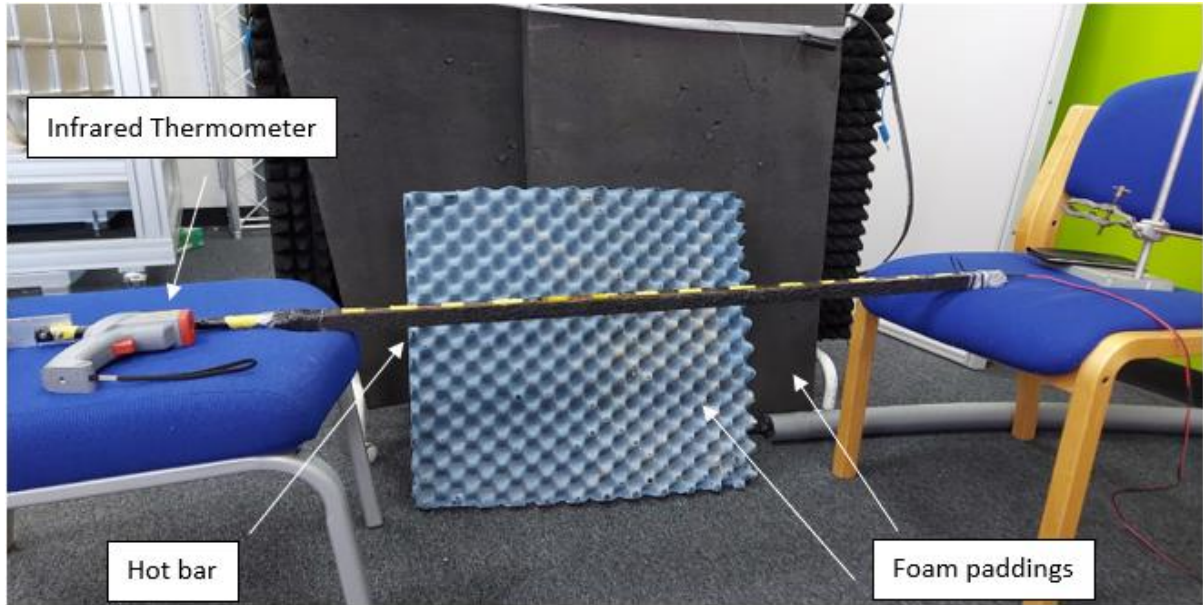


Figure 14 Set up of hot bar electrically heated with foam paddings behind

The temperature of the hot bar T_{hotbar} and the room temperature T_{room} was measured using an infrared thermometer, which was found to be:

$$T_{hotbar} = 41.3 \pm 0.1^{\circ}C$$

$$T_{room} = 22.7 \pm 0.1^{\circ}C$$

The detector was turned on and data taken for 5 seconds. It is important that the detector should take short timestream data as temperature fluctuations in the detector is significant. Implications of thermal fluctuations are further explored in the Results and Discussion chapter.

The methodology will focus on KID 2, as it shows the clearest results to illustrate the data analysis methodology. The same procedures are done for all the detectors to characterize the array. The detector outputs timestream data of I and Q values, $I(t)$ and $Q(t)$ respectively. The timestream plot of $|S_{21}|$ for KID 2 is shown:

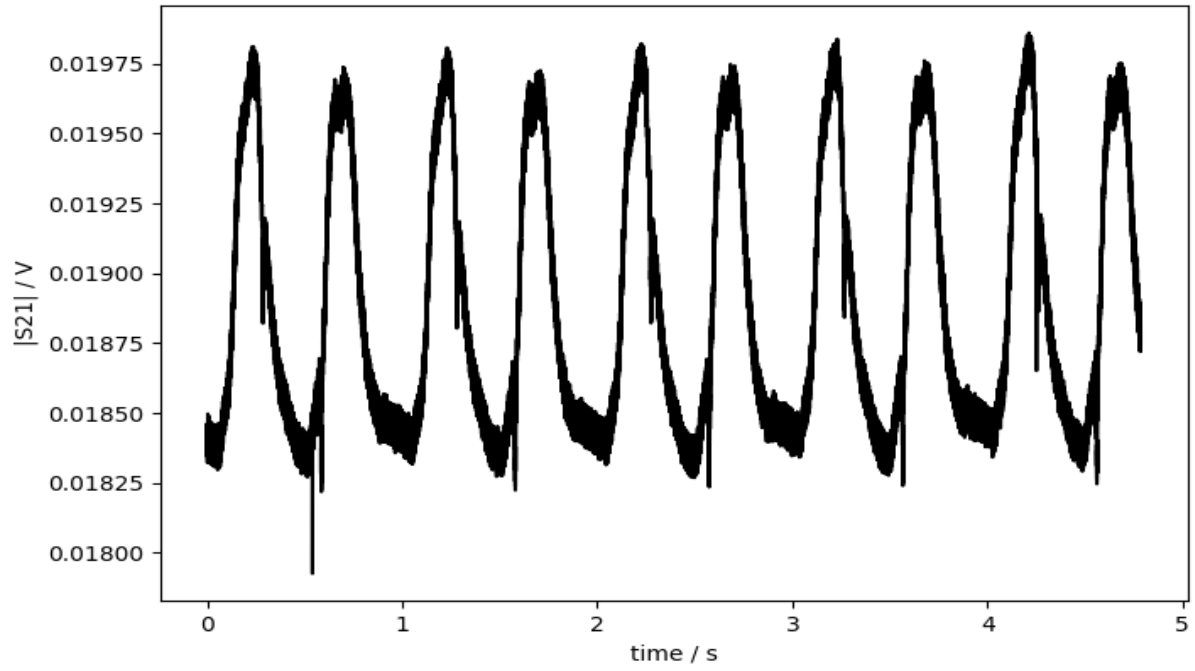


Figure 15 Graph of $|S_{21}|$ vs time for KID 2

Similarly, the detector with F_0 placed, will also output a frequency sweep:

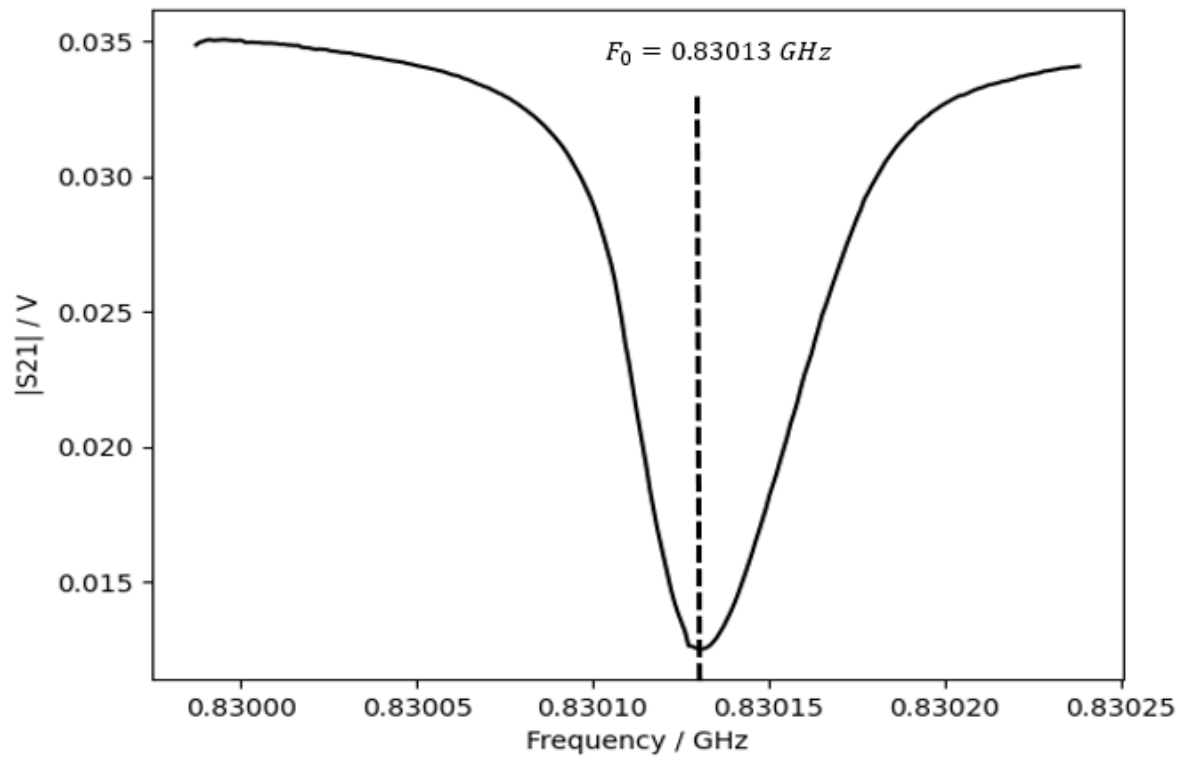


Figure 16 Graph of frequency sweep for KID 2 with F_0 placed at 0.83013 GHz

Using the I and Q values from the sweep data, the values of $\frac{dI}{dF}$ and $\frac{dQ}{dF}$ can be calculated at the minimum of the curve at F_0 . Following this, the values of $\partial I(t)$ and $\partial Q(t)$ can be found using the following expressions:

$$\partial I(t) = I(t) - I(F_0) \quad (26)$$

and

$$\partial Q(t) = Q(t) - Q(F_0) \quad (27)$$

Where $I(F_0)$ and $Q(F_0)$ are I and Q values at F_0 respectively. Inputting $\partial I(t)$, $\partial Q(t)$, $\frac{dI}{dF}$ and $\frac{dQ}{dF}$ into Equation 25 gives the timestream data for ∂F_0 . The plot of ∂F_0 vs time is shown:

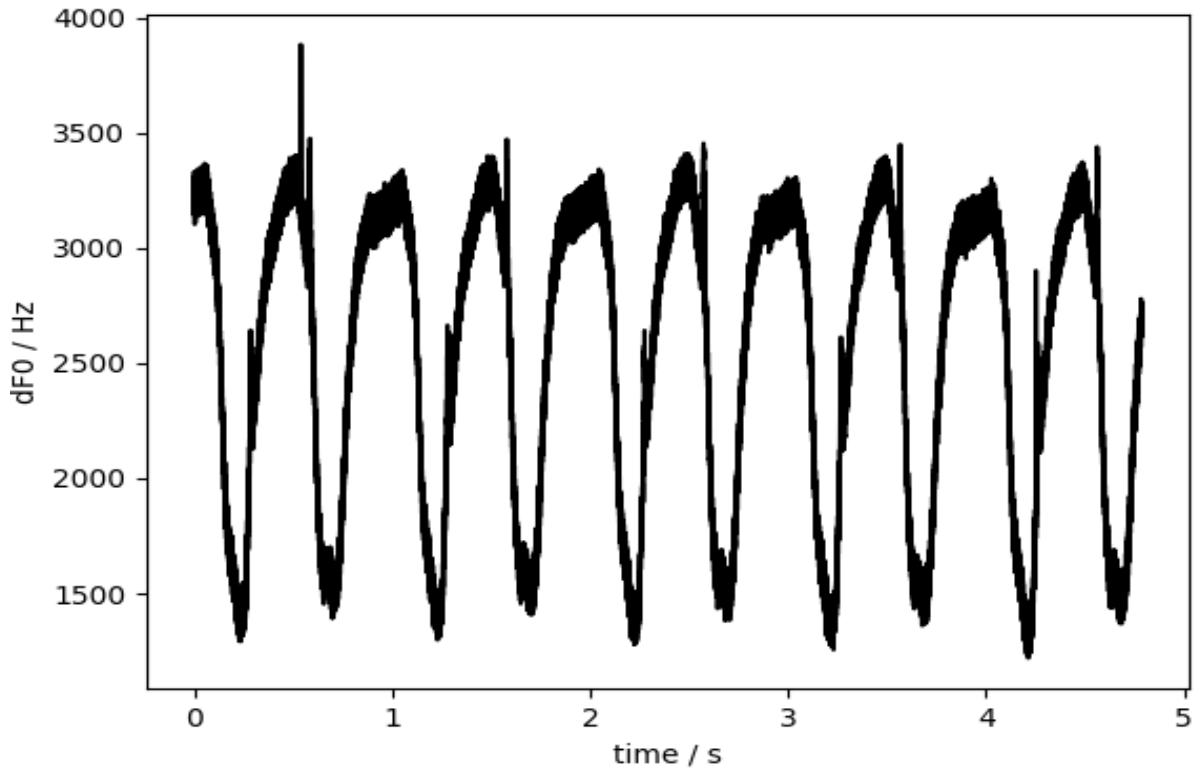


Figure 17 Graph of ∂F_0 vs time calculated using the dF_0 formula

The timestream data of ∂F_0 is useful for calculating R as the peak heights corresponding to the hot bar is the dF_0 . This is explored in section 3.3.

3.2 Modelling the Hot Bar Power, dP

Before the responsivity R of the detector can be calculated as shown in *Equation 1*, dP needs to be found first. Since the hot bar is of known temperature T_{hotbar} , it is possible to model the hot bar as a blackbody emission to find its blackbody intensity.

Detector System Filters

The power incident on the detector is limited by the filters of the KID system, which are shown in the schematics below:

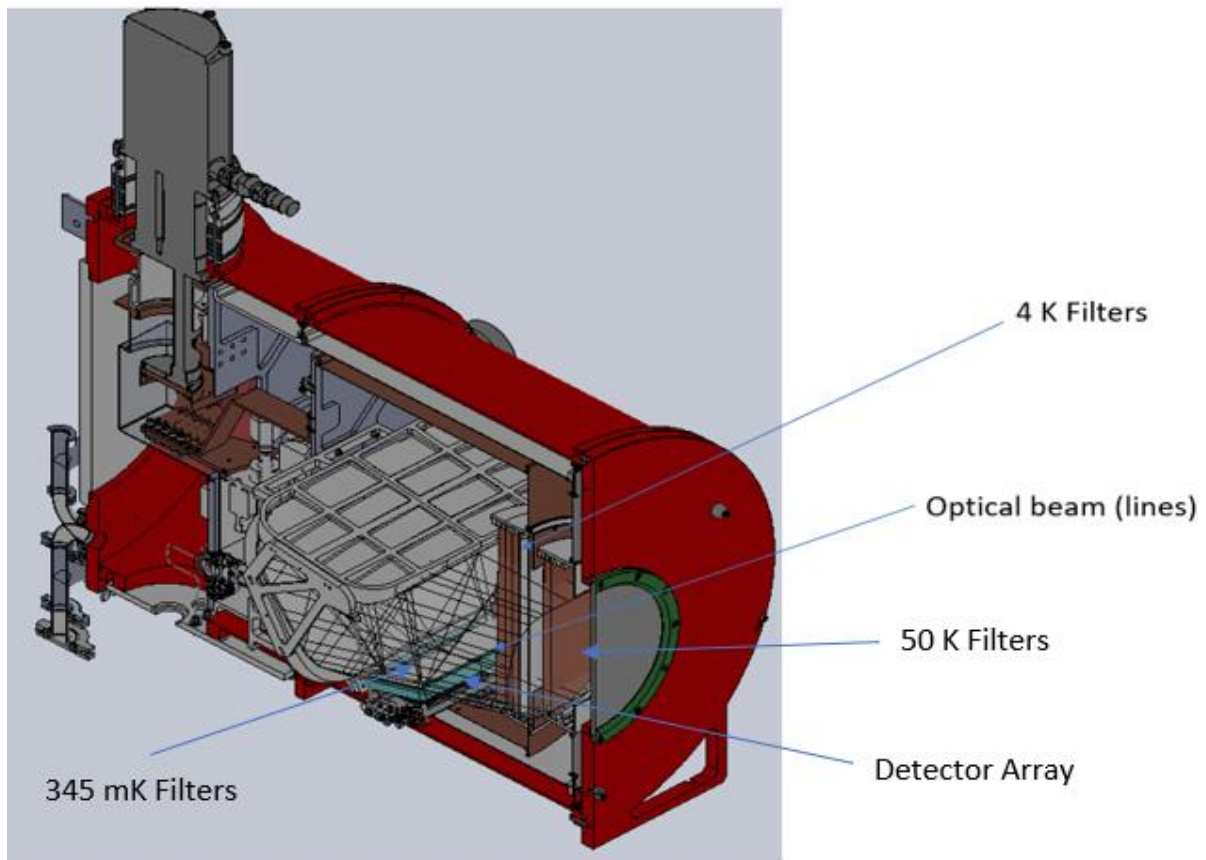


Figure 18 [22] Schematic of the camera interiors with the filters labelled

These filters were placed to limit the allowed frequency to the frequency range that is of interest in airport security cameras. This is because the larger the bandwidth, the larger the noise power let in, since the detector accepts a wider undesired frequency range.

The optical transmission spectrum for all the filters combined was provided by Dr. Sam Rowe, the transmission fraction spectrum is shown:

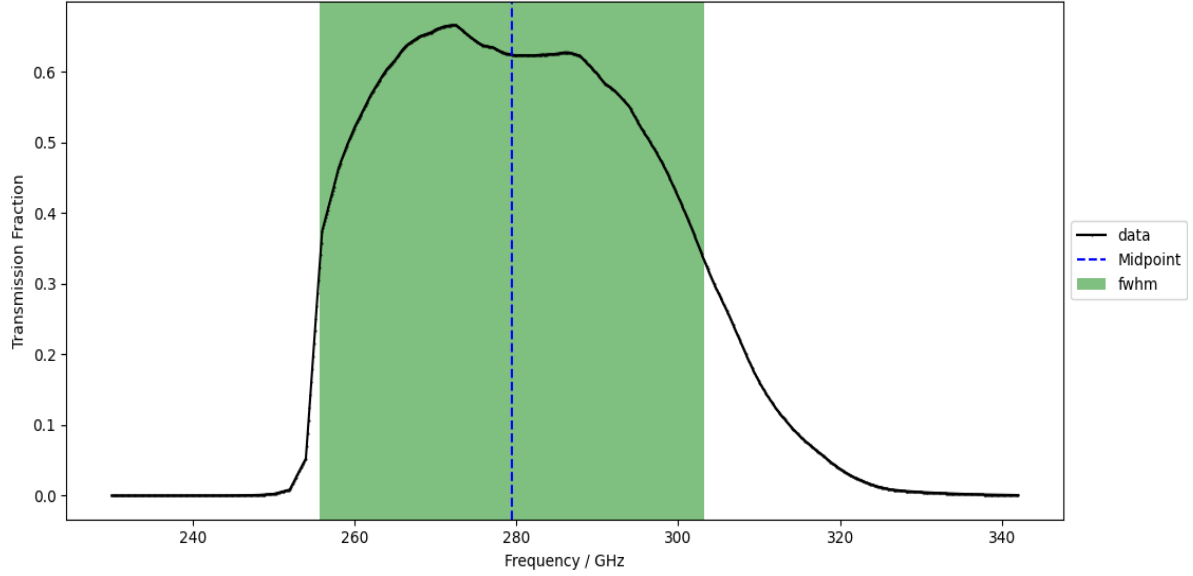


Figure 19 Graph of transmission fraction spectrum for the filters, where the full-width-half-maximum (fwhm) is denoted by the green bar and the blue line is the midpoint of the curve

The midpoint and full-width-half-maximum (fwhm) of the curve was found to be:

$$\text{Midpoint} = 279.5 \text{ GHz}$$

$$\text{fwhm} = 47.5 \text{ GHz}$$

The midpoint frequency equates to a wavelength of 0.00107m. The fwhm will be used later in the results and discussion section to calculate the total photon noise. The filter response $\alpha(\nu)$, in the data range df of width 112 GHz spanning from 230 – 342 GHz, will be used to estimate the blackbody passed by the filters.

All frequencies outside of df is assumed to have transmission fraction of 0, as the filters should in principle prevent the optical powers outside the range to reach the detector.

Hot Bar Power dP

Planck's Radiation Law gives the relationship between the spectral density B , which describes the spectral emissive power per unit area A , per unit solid angle Ω , for frequency ν and the temperature T [13]:

$$B(\nu, T) = \frac{2h\nu^3}{c^2(\exp(\frac{h\nu}{k_B T}) - 1)} \quad (28)$$

Where k_B is the Boltzmann Constant, h is the Planck Constant and c is the speed of light in vacuum.

Since B is per unit area A , per unit solid angle, B needs to be integrated over $d\Omega$ and dA to obtain the power. To simplify, the detector can be modelled as a directional antenna with a narrow beam making it beam filling as the narrow beam is filled by the source. As such, the Ω for beam-filling antennas is given as [23]:

$$\Omega \approx \pi \left(\frac{1.2\lambda}{2D} \right)^2 \quad (29)$$

Where D is the diameter of the antenna and λ is the wavelength. Following this, the effective area of detector A_e is approximated as the geometrical area of circle:

$$A_e \approx \frac{\pi D^2}{4} \quad (30)$$

From this, the throughput of the detector β is defined as $\beta = \Omega A_e$ [23]. Substituting Ω and A_e using Equation 29 and 30 gives:

$$\beta = \left(\frac{\pi D^2}{4} \right) \pi \left(\frac{1.2\lambda}{2D} \right)^2 \approx \lambda^2 \quad (31)$$

The expression $\beta = \lambda^2$ holds for all types of antennas and can be used in place of ΩA_e [23]. The value of λ is taken as the midpoint of the curve in Figure 19, and this gives $\beta = 1.1505 \times 10^{-6} m^2$.

It is now possible to calculate the hot bar signal power incident on the detector P . P was found by integrating Equation 29 over dv for $T = T_{hotbar}$ multiplied by the transmission fraction as a function of frequencies $\alpha(v)$ and the throughput λ^2 :

$$P(T_{hotbar}) = \beta \int_{v_2}^{v_1} \alpha(v) B(v, T_{hotbar}) dv \quad (32)$$

Inputting T_{hotbar} , β , $\alpha(v)$, between limits $v_1 = f_1$ and $v_2 = f_2$ in Equation 32 gives:

$$P = 2.6105 \times 10^{-10} W$$

Note the distinction that P is the modelled power incident on the detector and not the actual hot bar power dp . This is because P considers both the blackbody radiation of the hot bar and the background. Subtracting the power of background $P_{background}$ from P gives dP :

$$dP = P - P_{background} \quad (33)$$

$P_{background}$ can also be modelled as a blackbody radiation at temperature $T_{background}$ for dv between f_1 and f_2 . Using Equation 32, $P_{background}$ was found to be:

$$P_{background} = 2.4527 \times 10^{-10} \text{ W}$$

Using $P_{background}$ and P in Equation 33 gives:

$$dP = 1.9800 \times 10^{-11} \text{ W}$$

3.3 Detector Response

Measuring dF_0

From Figure 17, the peaks corresponding to the hot bar readings was identified to be the smaller peaks in the timestream data, illustrated in the diagram below:

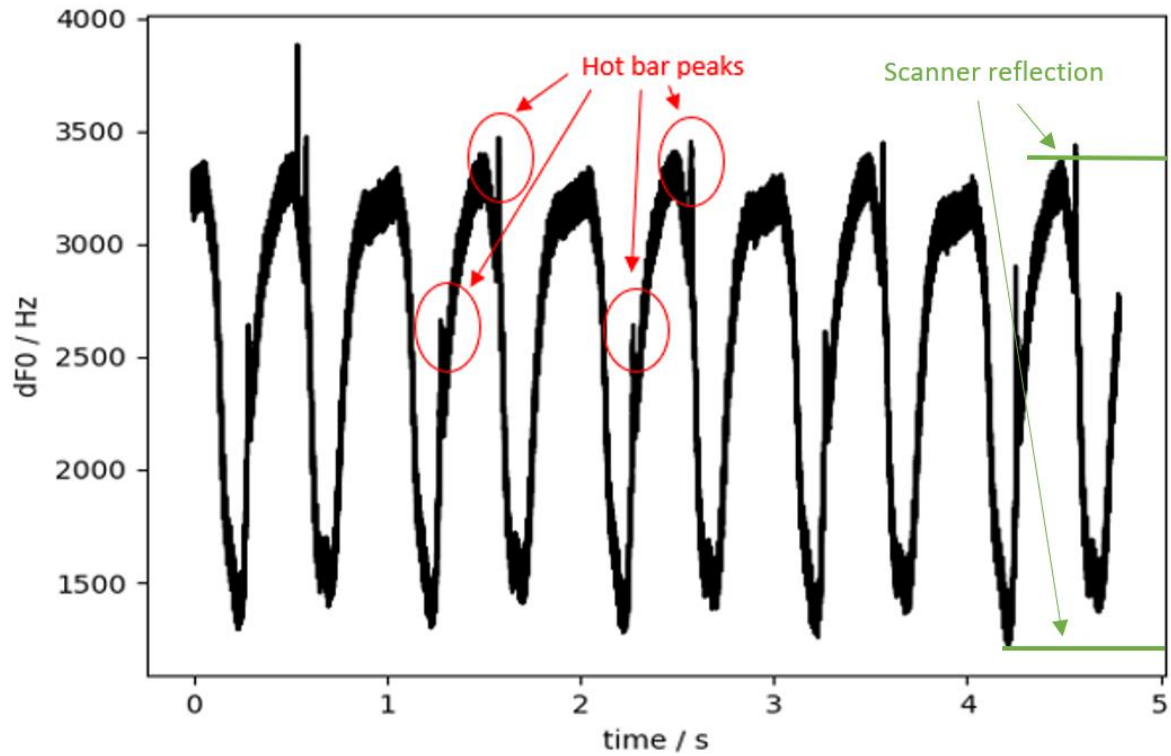


Figure 20 Graph of dF_0 vs time for KID 2, with the hot bar peaks and scanner reflection highlighted

Figure 20 shows that features oscillate, which is due to the detector scanning continuously up and down. Since T_{hotbar} is higher than T_{room} , the hot bar must have a peak on the graph as the detector scans across it. The large oscillating peaks are not the hot bar, they correspond to the reflection on the camera window. The only other peaks are the small peaks, which belong to the hot bar. A zoomed in of the small peak at $\sim 1.58s$ is shown:

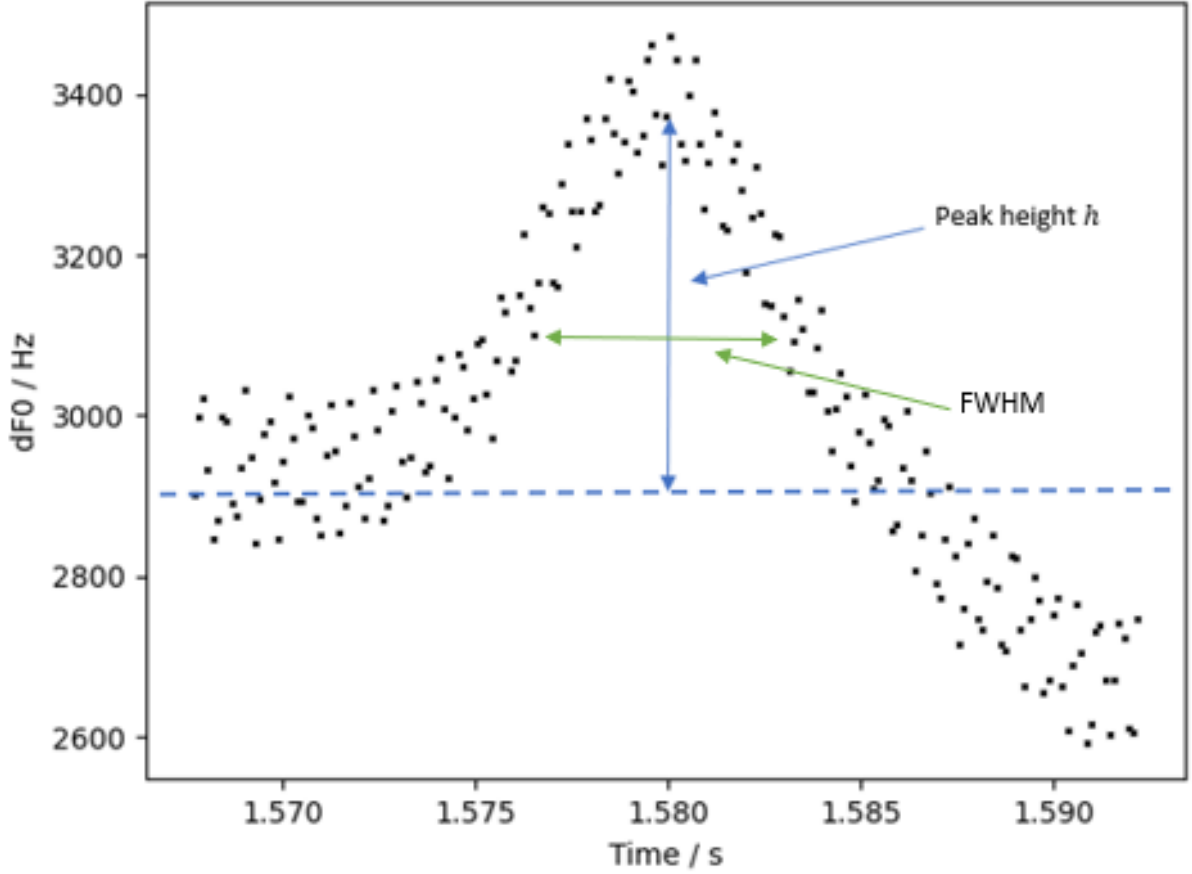


Figure 21 Graph of ∂F_0 vs time zoomed in for the hot bar peak at $\sim 1.58s$, with the height of the peak and full-width-half-maximum (FWHM) labelled

The dF_0 for the hot bar is simply the height of the peak, h . Intuitively and from observation, the peak can be fitted with a Gaussian Distribution. The Gaussian Distribution has the general form in terms of mean μ , height h , offset y_0 , and standard deviation σ [24]:

$$f(x) = y_0 + h \exp\left(-\frac{(x - \mu)^2}{2\sigma^2}\right) \quad (34)$$

The Gaussian shape is due to the detector beam pattern where σ is the FWHM of the beam, h is the maximum response, μ is the time the peak was reached and y_0 is the offset in F_0 . Equation 34 was curve fitted to the data points in Figure 21, and the resulting plot is given:

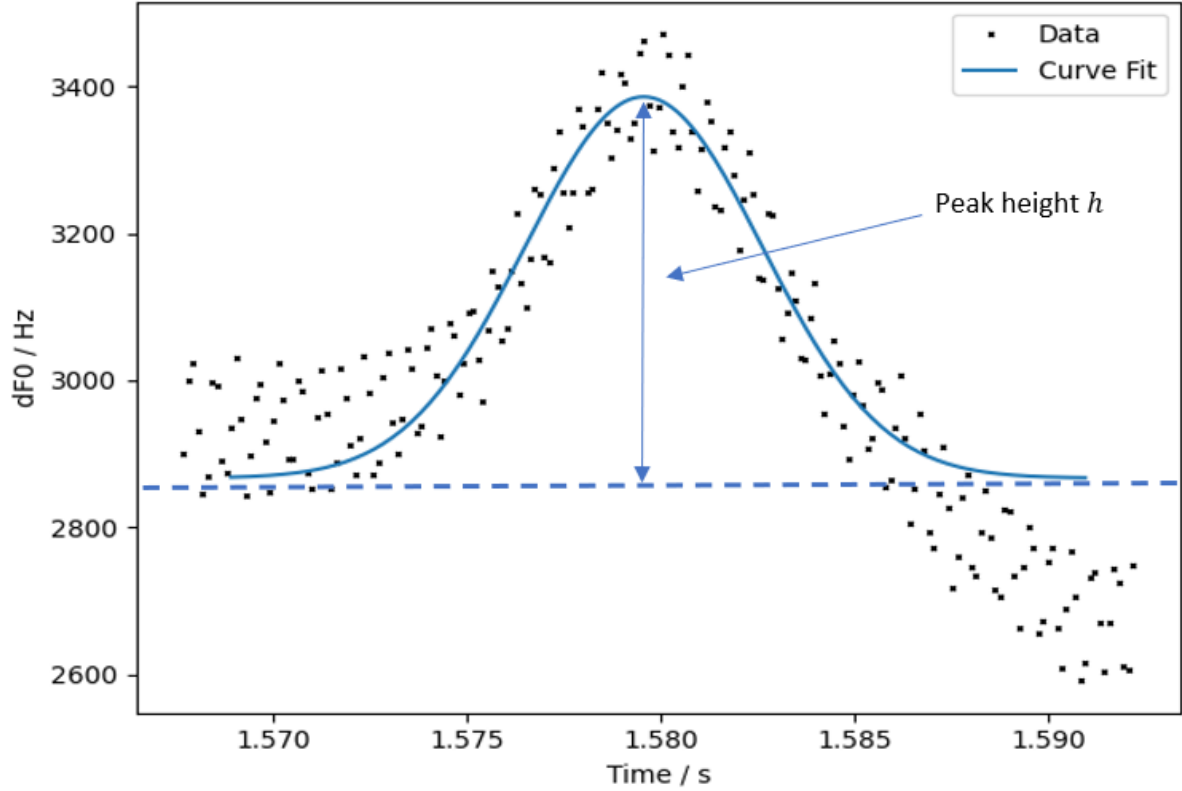


Figure 22 Gaussian curve fit for ∂F_0 data points of the peak of the hot bar

The fitting parameters for μ , h , σ and y_0 was found to be:

$$\mu = 1.5795 \text{ s}$$

$$h = 519.2 \text{ Hz}$$

$$\sigma = 0.00306$$

$$y_0 = 2866.8 \text{ Hz}$$

The dF_0 of the hot bar is therefore the peak height h , centred at $t = 1.5795\text{s}$, $dF_0 = 519.2 \text{ Hz}$. Comparing with the maximum variation allowed for ∂F_0 formula, determined from Figure 12, it can be said that the dF_0 is still valid.

Beam-Filling Factor (BFF)

The dF_0 calculated is an overestimate due to BFF. The BFF is defined as the fraction of the detector beam that is filled by the source. Since P was assumed to be beam-filling, the peak height of the curve overestimates the dF_0 for the hot bar as the beam is actually larger than the diameter of the hot bar. A visual illustration of the scenario is given:

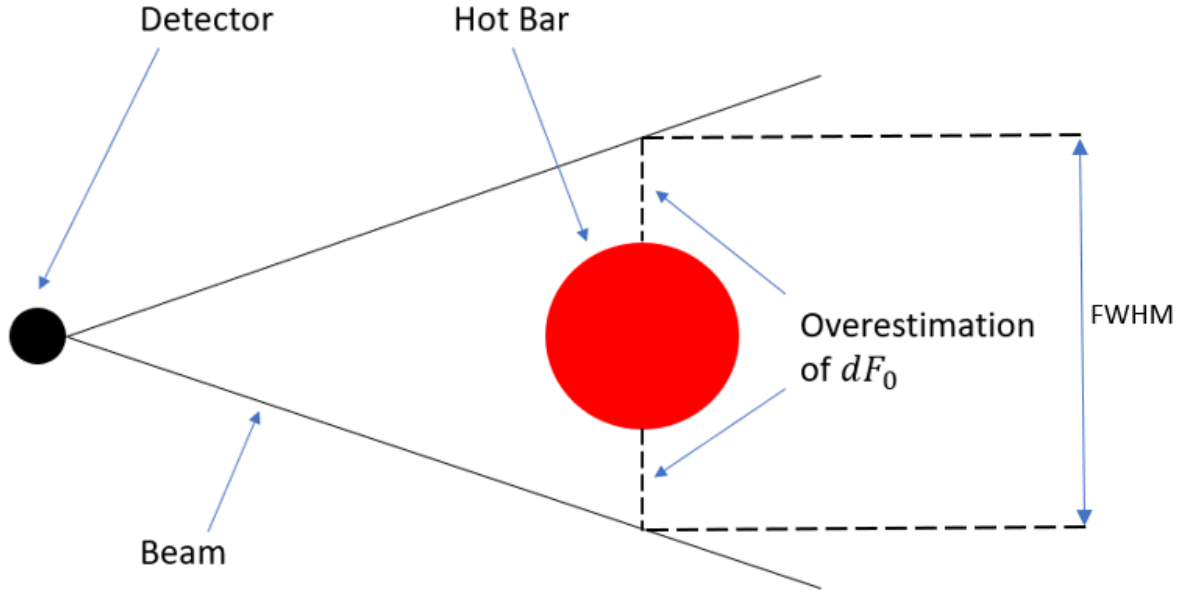


Figure 23 Diagram of the illustrating how dF_0 is overestimated

Figure 23 illustrates how the source does not fully cover the Ω of the beam. As such, the dF_0 found includes a response that is not from the hot bar. This is evident in Figure 22 as the peak for dF_0 does not plateau; since if it was beam-filling, dF_0 will be constant and the peak will flatten as the detector scans across it.

To determine the BFF, the intensity on the detector can be modelled as a 2D-Gaussian based upon the calculated beam width projected across the plane of the hot bar, where the hot bar would be a rectangle across it of width W . The 2D Gaussian was modelled for $100 \times 100 \text{ mm}$ square area since 100mm is the length of the hot bar. The fwhm of the 2D-Gaussian is the diameter of the circle which has area S subtended by the beam of solid angle Ω gives [23]:

$$\Omega = \frac{S}{d^2} \quad (35)$$

Where d is the distance of the hot bar to the detector. Combining Equation 29 and 35, inputting λ as the midpoint found from Figure 19, $D = 10\text{mm}$, and d measured to be 20m, the fwhm was calculated to be 20mm. This fwhm was used for the Gaussian and it was centred at the middle, with coordinates $x = y = 50\text{mm}$. This is illustrated below:

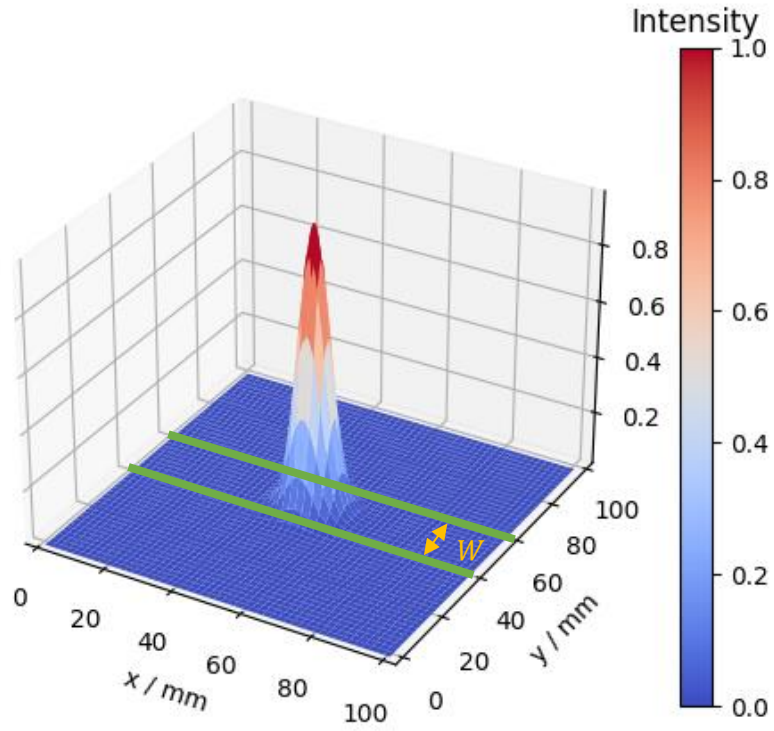


Figure 24 Side view of the 2D-Gaussian of photon intensity incident on the detector. The green lines denote the hot bar

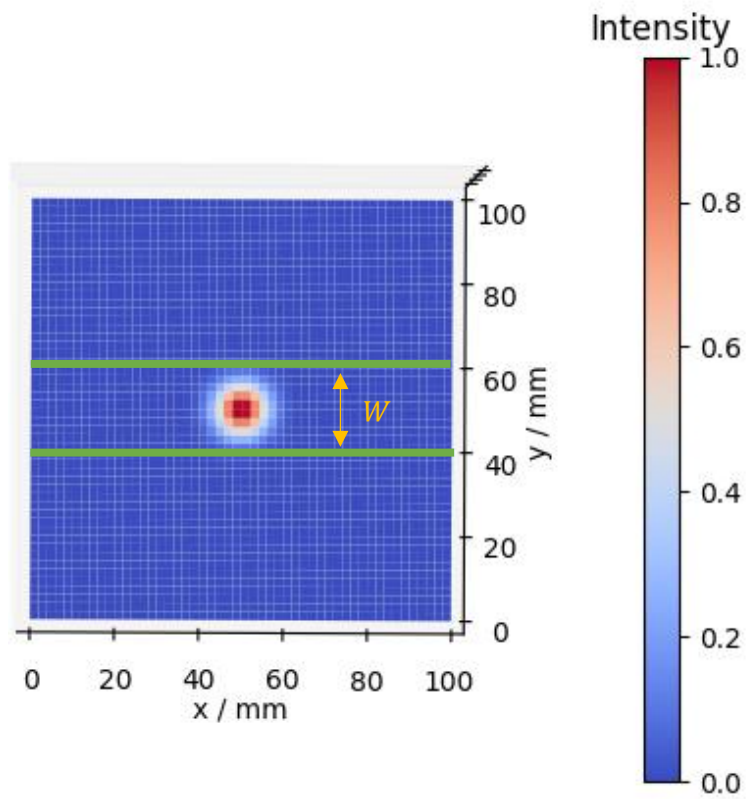


Figure 25 Top-down view of the 2D Gaussian of photon intensity incident on the detector. The green lines denote the hot bar

The BFF can be calculated as a ratio between the integral of intensities I within the hot bar dimensions over the integral to I of the Gaussian distribution:

$$BFF = \frac{\iint^{Hotbar} I \, dx \, dy}{\iint I \, dx \, dy} \quad (36)$$

W was measured to be $20mm$, leading to BFF of:

$$BFF = 0.9848$$

Responsivity R

R of KID 2 can now be found by using *Equation 1* along with the BFF:

$$R = \frac{dF_0(BFF)}{dP} \quad (37)$$

Using the values for dF_0 , BFF and dp , the value of R was calculated to be:

$$R = 2.622 \times 10^{13} \, HzW^{-0.5}$$

R of KID 2 has been quantified, which was part of the aims and objectives of this report. R allows for NEP calculations for further analysis in the following section.

3.4 Noise-Equivalent-Power

Noise Spectral Density e_n

Using *Equation 3*, the noise spectral density e_n and R is used to calculate the NEP. R has been calculated, but e_n has not. As mentioned, e_n is the noise power density per unity Hz of bandwidth. This can be calculated by taking the Fourier Transform of the ∂F_0 timestream obtaining e_n for each Hz bin. Using the SciPy package in Python, the Fourier Transform of the ∂F_0 was found, and the resulting e_n vs frequency plot created:

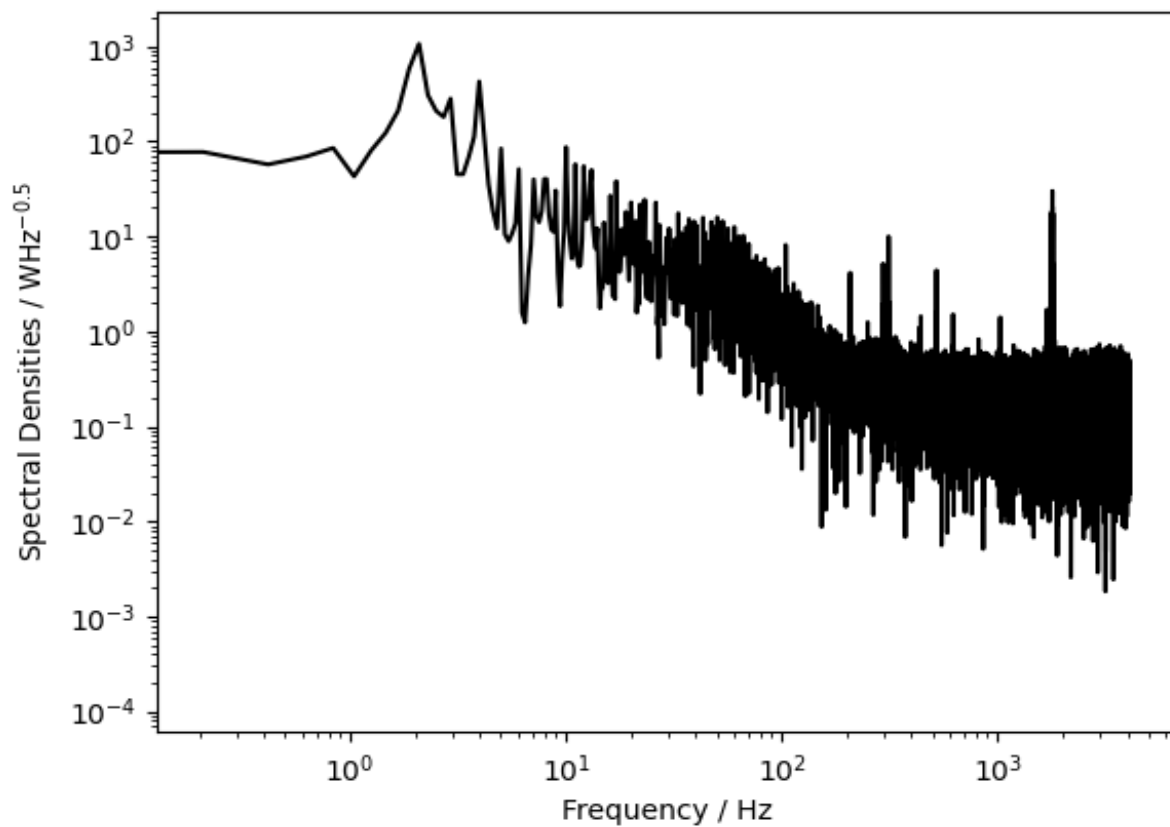


Figure 26 Loglog plot of spectral density vs frequency of KID 2 ∂F_0 data

The Noise Spectral Density is one of the performance metrics in the aims and objectives of this report. Analysis of the noise can be performed on this spectrum, and this can provide an insight into the sources of noise from *Figure 26*, further discussed in the Results and Discussion section.

Noise-Equivalent-Power (NEP)

The NEP as described in the Introduction section, is the minimum detectable power, limited by the noise power. The NEP can be calculated using *Equation 3* using the e_n calculated and R , which gives a resulting plot shown below:

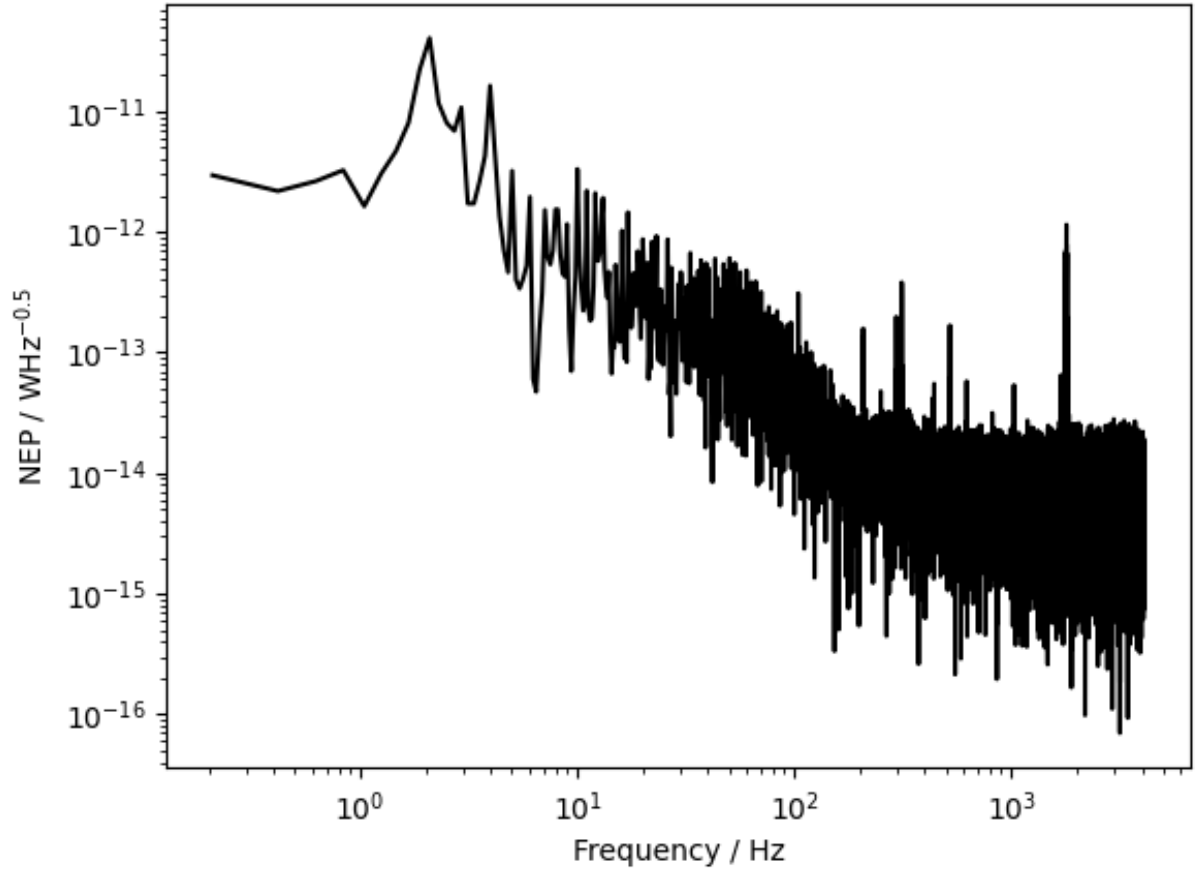


Figure 27 Loglog plot of NEP vs frequency for KID 2

Figure 27 is one of the aims and objectives of the report, which is to characterize the NEP of a KID. However, the main aim is to characterize the whole array. As such, the NEP distribution for all the KIDs need to be determined and a histogram of all the KIDs average NEP can be plotted to characterize the array.

NEP Distribution for the Detector Array

To compare with the photon noise limit, which is the fundamental limit, the average NEP of the array needs to be determined. The photon noise has the features of “white” noise, which has e_n that is constant over across frequency. The range that NEP can be observed to be constant is towards the higher frequency range from Figure 27. As such, the average “white” NEP level NEP_{white} can be found by taking an average of the NEP over this range. An annotated graph of the NEP is shown for finding NEP_{white} for KID 2:

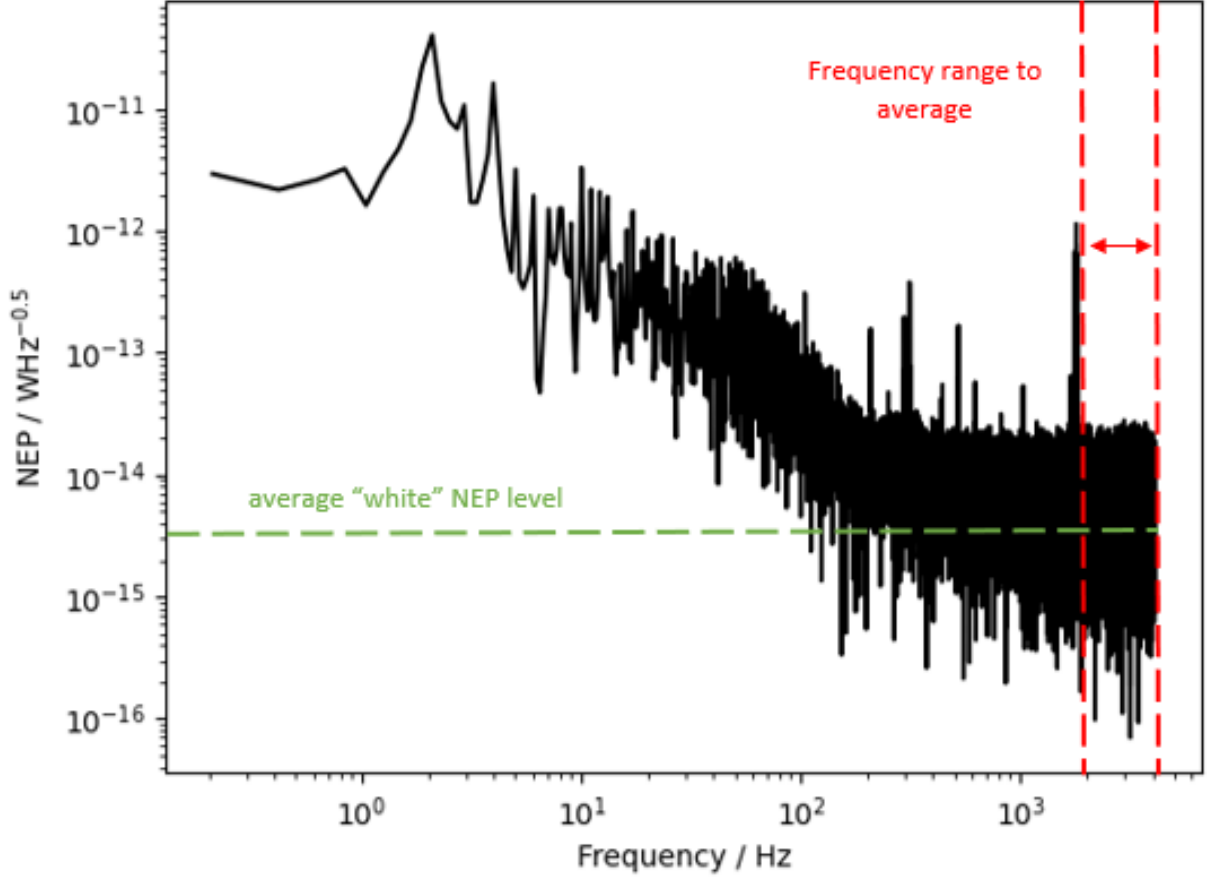


Figure 28 Loglog plot of NEP vs frequency for KID 2, the green line denotes the NEP_{white} level, and red denotes the higher frequency range to average. The NEP values bounded by the red lines can be observed to be constant, making it a “white” NEP level

The frequency range labelled in red for Figure 28 is between 2000 - 4000 Hz. The average NEP NEP_{white} for this range is:

$$NEP_{white} = 2.50 \times 10^{-15} \text{ WHz}^{-0.5}$$

NEP_{white} will be used to compare with the photon noise limit since the photon noise has a white feature, so KID’s NEP NEP_{KID} is taken to be NEP_{white} . However, it should be noted that the white noise is comprised of other sources of noise. The implications of this are further discussed in the Results and Discussion section.

The procedures for calculating dF_0 , R , e_n , NEP and the NEP_{KID} is done for all the other 113 KIDs that had data outputs. The resulting histogram plot of NEP_{KID} is given below:

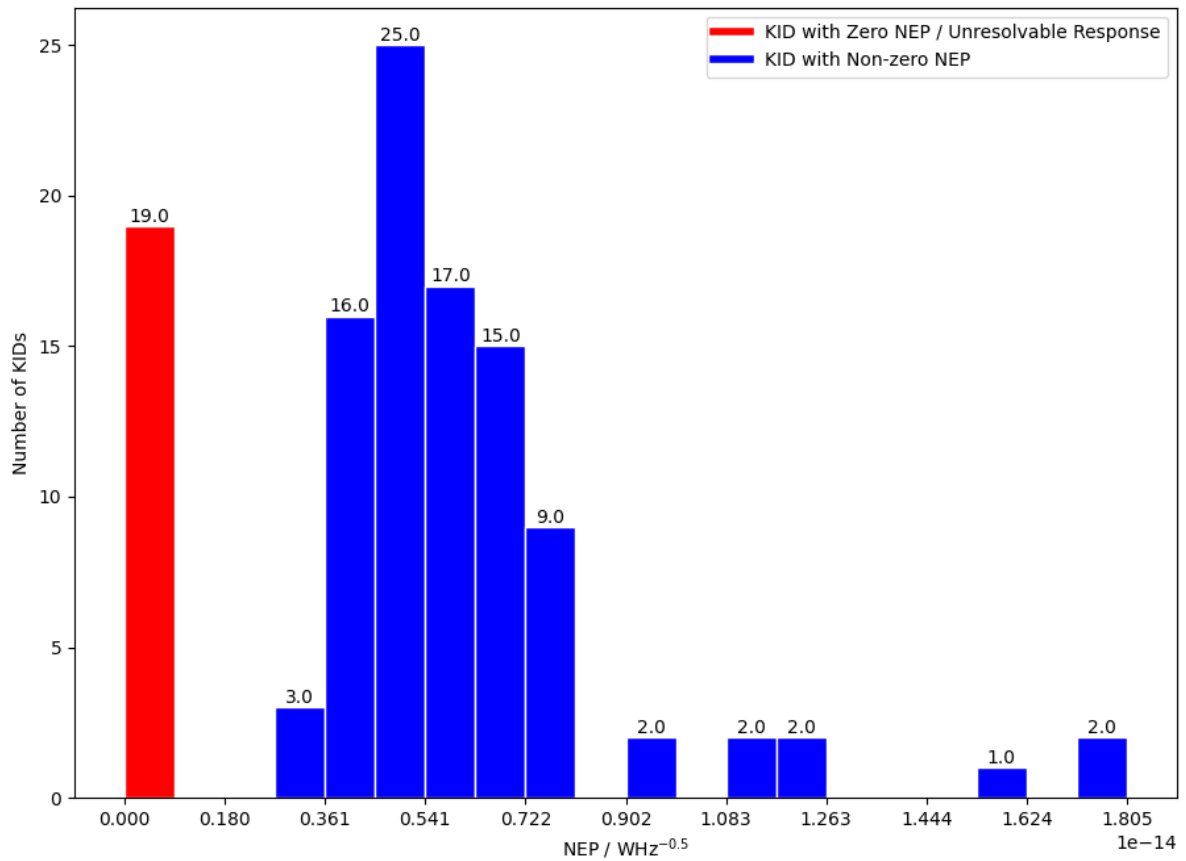


Figure 29 Histogram of NEP of all 113 KIDs that had data output in the array

The histogram is a part of the aims and objectives for the report, where the final step is to compare it with the fundamental noise limit, which is further explored in the Results and Discussion section

4. Results and Discussions

4.1 Analysis of Results

Total Photon Noise

The photon noise is the uncertainty associated with measuring light due to the quantized nature of light and how each photon is treated independently [13]. The photon noise has 2 contributions: photon shot noise and photon wave noise.

- Photon Shot Noise

Since the photons are quantized and independent, there are no correlation between the arrival of one photon and another. This leads to a random fluctuation of the arrival rate of photons on the detector, this is defined as the shot noise which is given by [13]:

$$Shot\ Noise = \sqrt{2P_{BG}h\nu} \quad (38)$$

Where P_{BG} is the background power. ν is the midpoint frequency of the spectrum.

- Photon Wave Noise

From quantum mechanics, it is more appropriate to treat light as a wave instead of photon stream at low frequencies. The previous treatment using photon shot noise needs to be modified to take this into account by taking the arrival of wave peaks instead of photons, this is attributed to the wave noise [23]. The full derivation of the wave noise is beyond the scope of this project, and only the final expression is needed. Quoting from [23] that uses a full Bose-Einstein treatment will give the expression for the wave noise:

$$wave\ noise = \frac{P_{BG}}{\sqrt{2d\nu}} \quad (39)$$

To add 2 noise sources, they must be added as a quadrature sum [14]. Combining both shot and wave noise gives the expression for the total photon noise NEP_{total} :

$$Total\ Photon\ Noise = \sqrt{wave\ noise^2 + shot\ noise^2} \quad (40)$$

Using Equation 38, 39, and 40 along with the values of $P_{BG} = P_{background}$, where dv and ν is the fwhm and midpoint frequency of the filter transmission found in Figure 19 respectively, gives the total photon noise:

$$Total\ Photon\ Noise = 8.511 \times 10^{-16} WHz^{-0.5}$$

Comparing KID array NEP with total photon noise

The mean NEP of the array NEP_{array} can be found by taking the mean of the histogram in Figure 29 which has a Gaussian shape. However, there is insufficient data points for a curve fit to be done. As such, the mean is approximated to be at the midpoint of the curve peak. This is shown in the graph below along with the total photon noise level:

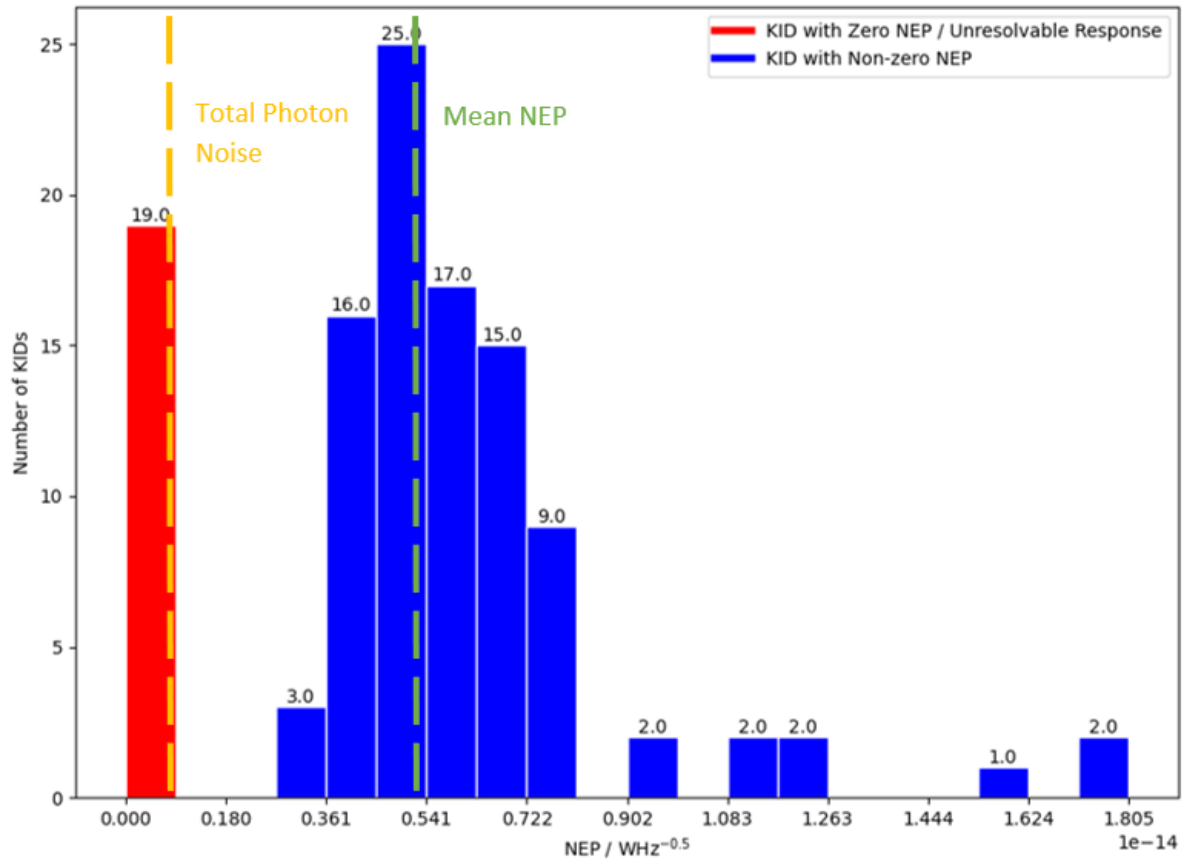


Figure 30 Histogram of KID array NEP, with mean NEP labelled by the green line and total photon noise labelled by the yellow line

From Figure 30, it can be observed that all the NEP of the KID array is higher than the total photon noise. This agrees with the understanding that the total photon noise is the fundamental noise limit, and there should not be any NEP values lower than this.

NEP_{array} was found to be:

$$NEP_{array} = (5.0 \pm 0.5) \times 10^{-15} \text{ } WHz^{-0.5}$$

By taking a ratio of $NEP_{array}/Total \text{ Photon Noise}$, how much larger the NEP_{array} is to the total photon noise can be quantified. This ratio was found to be 5.88, so NEP_{array} is 5.88 times larger than the total photon noise. Ideal detectors are photon noise dominated and have their array NEP equal to the photon noise limit. Since the system is not ideal, this result makes sense. This is further explored in the following section to explain why the experimental NEP deviates from the photon noise limit.

4.2 Implications on the System

Comparisons with Different Detector Types

As mentioned previously, the performance metrics can be used to compare between detector types. In this section, NEP_{array} was compared with several detector types that operate within the mm-wave spectrum. For a fair comparison, since the SFAB system was developed for commercial use, the NEPs of commercially available detector types mentioned in the introduction section was used, shown in the following table, arranged in order of ascending NEP:

Detector Type	$NEP / pWHz^{-0.5}$
Kinetic Inductance Detector (SFAB)	0.0050
Semiconductor type	0.0164 [14]
Bolometer (TES)	0.38 [15]
Heterodyne Receiver	14.0 [16]

Table 2 NEP values for different commercial detector system of various type in the mm-wave spectrum listed in ascending order

The lower the NEP, the more sensitive the detector system. From *Table 2*, the SFAB system is shown to have a lower NEP compared to other commercially available detectors. This implies that it is easier to create KID systems of higher sensitivity, which confirms that KIDs create highly sensitive systems easily.

Detector Yield

From the introduction section, the detector yield is defined as the ratio of the number of KIDs that gave a response $n_{responsive}$ to the total number of KIDs n_{KID} . The SFAB has 2 arrays, giving a total of 174 KIDs.

From *Figure 30*, $n_{responsive}$ can be determined from the sum of blue bars. The red data, although outputted data, is considered not responsive, as no response can be identified. This number was found to be:

$$n_{responsive} = 94$$

Using $n_{responsive}$ and n_{KID} in *Equation 4*, the detector yield was found to be:

$$Yield = 53.4\%$$

The detector yield calculated is quite low, as this implies that almost half the detectors in the array did not give a resolvable response. The detectors that did not give data could be attributed to many physical problems such as excess temperature fluctuations, uncoupled detectors, damage, etc. The exact determination is beyond the scope of the project.

The remainder of the KIDs gave an unresolvable response, as shown by the red data in *Figure 30*. This is due to excess noise that masks the hot bar response, which led to an unresolvable response for those detectors. The cause of this can be attributed to several sources, but the exact determination is beyond the scope of the project.

4.3 NEP Contributions and Noise Sources

NEP_{array} was found to be 5.88 times larger than the total photon noise. This is mainly caused by excess noise on the detector and underestimation of response. This section focuses on analyzing and identifying the cause for increased NEP_{array} compared to the photon noise.

Underestimation of dF_0

One potential reason why the NEP_{array} is higher is due to an underestimation of R , which could be due to dF_0 being underestimated. There are several factors that cause this, but mainly attributed to the intensity loss of the photons on its journey from the hot bar until it reaches the detector.

One major source of this loss is at the lenses of the detector. The signal gets attenuated by the refractive index change of the lens from air which causes more of the photons to be refracted and not reach the detector.

Overestimation of dP

Another factor that affects R is dP being overestimated. This is due to modelling the hot bar as a perfect blackbody. Real radiation is not perfect, the hot bar cannot be modelled as a perfect blackbody. The intensity of radiation I_ν is thus [23]:

$$I_v = \varepsilon(\nu)B(T) \quad (41)$$

Where $\varepsilon(\nu)$ is the emissivity of the material surface.

As an example, assuming the material of the hot bar is entirely oxidized steel, ε for oxidized steel is [25]:

$$\varepsilon_{steel} = 0.79$$

This implies that dP may be 21% higher than the actual dP , leading to a lower R .

However, the actual hot bar material is not as just a uniform material. *Figure 14* shows that the hot bar surface is a composition of materials with different ε , and determining the ε is beyond the scope of this project. As such, a perfect blackbody is assumed.

Noise Sources and Excess NEP Contributions

As previously mentioned, the features of noise sources can be characterized from the noise spectral density graph. The following different noise features can be identified from *Figure 26*, and the noise sources inferred:

- White Noise

Defined as the noise in which the power spectrum is constant and independent of frequency. [14]
This can be seen in the plot:

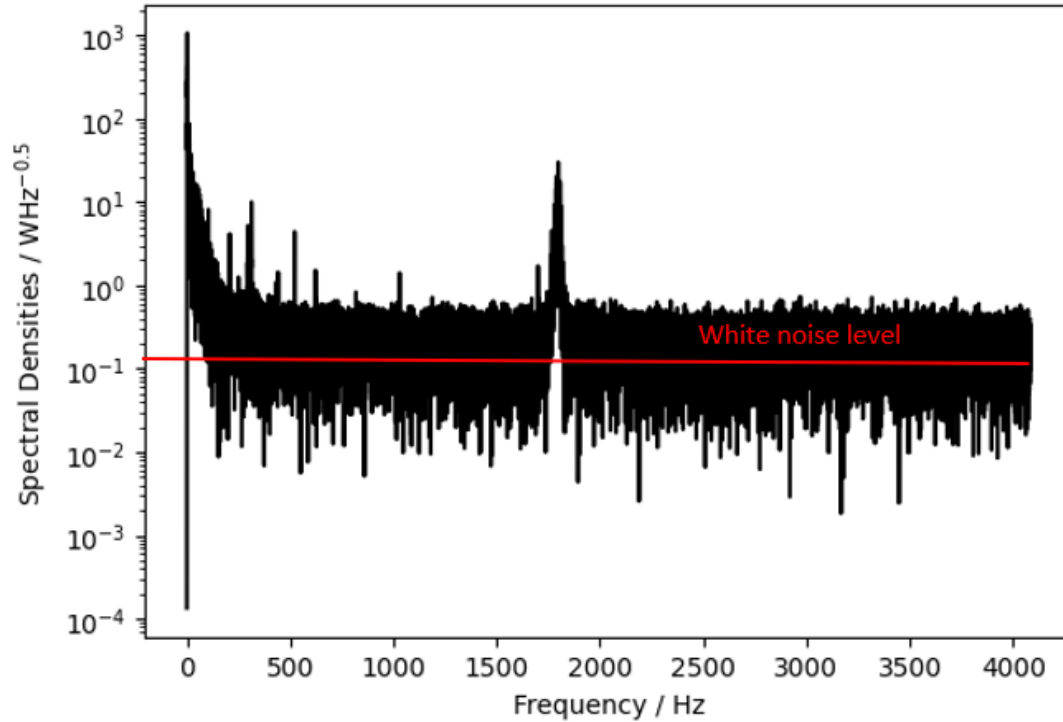


Figure 31 Semilog plot of e_n vs frequency, with the white noise level labelled by the red line

The source of the white noise is formed of a mixture of noise sources such as the thermal noise and photon noise, as they have constant e_n irrespective of frequency [14]. There is insufficient data to determine the exact contributions of all sources of the white noise.

As mentioned previously, there were implications of using the NEP_{white} to calculate NEP_{KID} . This is due to the thermal noise not being considered in calculations. The main source of this thermal noise is generated by the generation-recombination of the Cooper-pairs of the KID [7]. Since the KID was at ~ 270 mK, it will certainly have thermal agitation contributing to the thermal noise. Since the white noise is typically a mixture of thermal and photon noise, the thermal noise was not considered in the NEP_{array} calculation, which contributes to why NEP_{array} is higher than the total photon noise.

- $1/f$ Noise

The $1/f$ noise is defined such that the e_n is inversely proportional to the signal frequency [23], shown below:

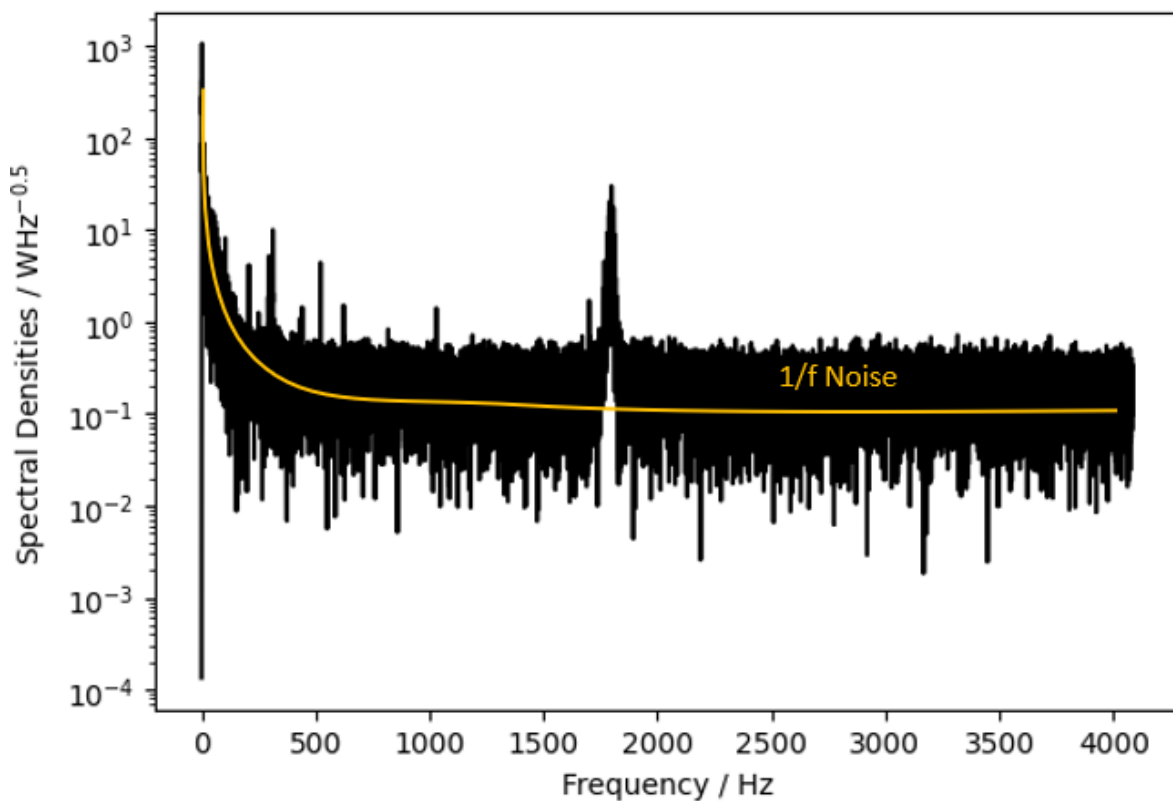


Figure 32 Semilog plot of e_n vs frequency, with the $1/f$ noise labelled by the yellow line

Figure 32 illustrates the $1/f$ noise, which falls with frequency. The source of the $1/f$ noise is formed of a mixture of noise sources, most dominantly the varying “scene” of the room as the detector

scans over it. Real world objects have non-uniform temperature distributions. As such, it causes small temperature variations, leading to a dF_0 response that has a $1/f$ feature. It is impossible to remove entirely, but can be limited. However, $1/f$ noise has limited effect on NEP since it was found at higher frequencies, whilst $1/f$ noise falls with frequency.

Interference

Wires and components in electrical circuits tend to act as antennas. They are able to pick up strong man-made signals (e.g. radio waves, 50 Hz mains, etc). An example is shown:

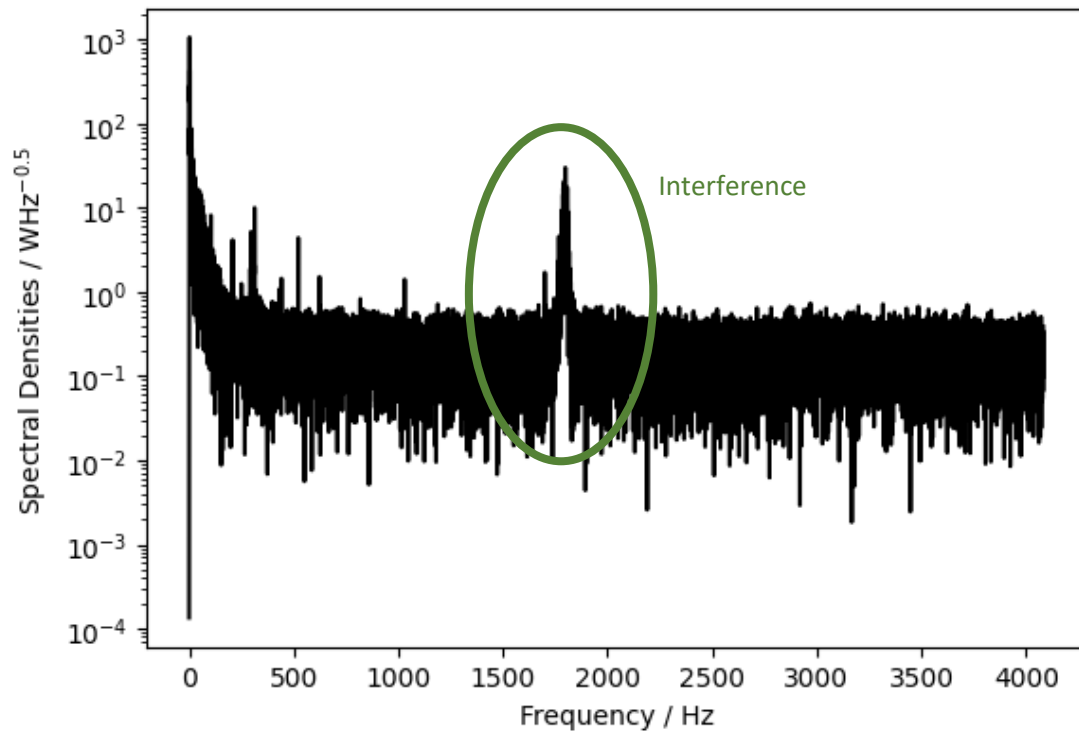


Figure 33 Semilog plot of e_n vs frequency, with the interference labelled by green

Figure 33 shows an interference e_n centred at 1800Hz, which could correspond to a signal from an electronic device. However, there is not enough information to determine the exact source of this interference. Since it is at a lower-mid frequency, it does not influence NEP_{array} since it was found by averaging at the higher frequency range.

5. Conclusions

The SFAB KID array has been characterized in terms of 4 detector properties in this report. The first property, the responsivity R of the KID was found to be $2.622 \times 10^{13} \text{ Hz/W}$. The noise spectral density e_n of a KID was characterized and the noise sources analyzed, where the total photon noise was found to be $8.511 \times 10^{-16} \text{ WHz}^{-0.5}$. From the noise spectrum and responsivity, a histogram of the NEP distribution of the KID array was generated and the array NEP was found to be $(5.0 \pm 0.5) \times 10^{-15} \text{ WHz}^{-0.5}$, which was 5.88 times larger than the photon noise limit, proving it is not photon noise limited. The reason was attributed to excess noise, underestimation of the dF_0 and overestimation of dP . The detector yield of the array was found to be 53.4%, the number of detectors that were responsive was 94, the detectors that did not have a resolvable response was 19 and the number of detectors that had no data was 64. Comparing with other commercially available detectors of different types within this wavelength shows that the KID array NEP is far lower than others, showing that it is easier to achieve higher sensitivity with KIDs. This shows that KIDs are a promising technology for mm-wave detection and has been shown to yield remarkable results in terms of its sensitivity and ease of creating large arrays.

6. References

- [1] National Academies of Sciences, Engineering, and Medicine. *Airport Passenger Screening Using Millimeter Wave Machines: Compliance with Guidelines*. National Academies Press, 2018
- [2] Daniels, Arnold. Field Guide to Infrared Systems, Detectors, and FPAs, Second Edition 10.1117/3.2315935, 2010
- [3] J. Bardeen, L. N. Cooper, and J. R. Schrieffer. Theory of Superconductivity. *Physical Review*, 108:1175–1204, December 1957
- [4] N. W. Ashcroft and N. D. Mermin. *Solid State Physics*. Saunders College Publishing, 1976.
- [5] F. London and H. London. The Electromagnetic Equations of the Supraconductor. *Royal Society of London Proceedings Series A*, 149:71–88, March 1935
- [6] C. J. Gorter and H. Casimir. On supraconductivity I. *Physica*, 1:306–320, 1934
- [7] S. Doyle, P. Mauskopf, J. Naylor, A. Porch and C. Duncombe. Lumped Element Kinetic Inductance Detectors. *Journal of Low Temperature Physics*, 151(1), 530-536, 2008
- [8] D. C. Mattis and J. Bardeen. Theory of the Anomalous Skin Effect in Normal and Superconducting Metals. *Physical Review*, 111:412–417, July 1958.
- [9] A. B. Pippard. An Experimental and Theoretical Study of the Relation between Magnetic Field and Current in a Superconductor. *Royal Society of London Proceedings Series A*, 216:547–568, February 1953.
- [10] D. M. Pozar. *Microwave Engineering*. Wiley, 2005.
- [11] Porch, A., Mauskopf, P., Doyle, S., & Dunscombe, C. Calculation of the characteristics of coplanar resonators for kinetic inductance detectors. *IEEE transactions on applied superconductivity*, 15(2), 552-555, 2005
- [12] B. A. Mazin. Microwave kinetic inductance detectors. PhD thesis, California Institute of Technology, United States – California, 2005
- [13] Hasinoff, Samuel W. "Photon, Poisson Noise." 608-610, 2014
- [14] Hyseni, Genc & Caka, Nebi & Hyseni, Kujtim. Infrared thermal detectors parameters: Semiconductor bolometers versus pyroelectrics. 9. 238-247, 2010
- [15] Mathias Kehrt, Christian Monte, Jörn Beyer, and Jörg Hollandt, "A highly linear superconducting bolometer for quantitative THz Fourier transform spectroscopy," *Opt. Express* 23, 11170-11182 (2015)
- [16] Grzyb, J., Pfeiffer, U. THz Direct Detector and Heterodyne Receiver Arrays in Silicon Nanoscale Technologies. *J Infrared Milli Terahz Waves* 36, 998–1032 (2015).

Non-academic Literature

- [17] S. Doyle, Slides: Introduction to Kinetic Inductance Detectors, 2016
- [18] Cooper pair energy, <http://hyperphysics.phy-astr.gsu.edu/hbase/Solids/coop.html>
- [19] Band gap energy, <http://hyperphysics.phy-astr.gsu.edu/hbase/Tables/Semgap.html>
- [20] S. Doyle, Understanding KID Microwave readout, 2021
- [21] S. Doyle, Schematics of KID, 2021
- [22] SFAB Schematics, Dr. Tom Brien
- [23] S. Doyle, PX3144 Electromagnetic Radiation Detection, Lecture Notes, 2021/22
- [24] Weisstein, Eric W. "Normal Distribution". Retrieved August 15, 2020.
- [25] Emissivity of steel, https://www.engineeringtoolbox.com/emissivity-coefficients-d_447.html